

APOGEE/*Kepler* Overlap Yields Orbital Solutions for a Variety of Eclipsing Binaries

JONI MARIE CLARK CUNNINGHAM,^{1,2} MEREDITH L. RAWLS,^{3,4} DIANA WINDEMUTH,³ ALEEZAH ALI,³ JASON JACKIEWICZ,⁵
ERIC AGOL,³ KEIVAN G. STASSUN,^{2,1}

¹*Department of Physics, Fisk University, Nashville, TN 37208*

²*Department of Physics and Astronomy, Vanderbilt University, Nashville, TN 37235*

³*Department of Astronomy, University of Washington, Seattle, WA 98195*

⁴*DIRAC Institute, University of Washington, Seattle, WA 98195*

⁵*Department of Astronomy, New Mexico State University, Las Cruces, NM 88003*

Abstract

Spectroscopic Eclipsing Binaries (SEBs) are fundamental benchmarks in stellar astrophysics and today are observed in breathtaking detail by missions like TESS, *Kepler*, and APOGEE. We develop a methodology for simultaneous analysis of high precision *Kepler* light curves and high resolution near-IR spectra from APOGEE and present orbital solutions and evolutionary histories for a subset of SEBs within this overlap. Radial velocities extracted from APOGEE spectra using the Broadening Function technique are combined with *Kepler* light curves and to yield binary orbital solutions. The Broadening Function approach yields more precise radial velocities than the standard Cross-Correlation Function, which in turn yields more precise orbital parameters and enables the identification of tertiary stars. The orbital periods of these seven SEBs range from 4 to 40 days. Four of the systems (KIC 5285607, KIC 6864859, KIC 6778289, and KIC 4285087) are well-detached binaries. The remaining three systems have apparent tertiary companions, but each exhibits two eclipses along with at least one spectroscopically varying component (KIC 6449358, KIC 6131659, and KIC 6781535). *Gaia* distances are available for four targets which we use to estimate temperatures of both members of these SEBs. We explore evolutionary histories in H-R diagram space and estimate ages for this subset of our sample. Finally, we consider the implications for the formation pathways of close binary systems via interactions with tertiary companions. Our methodology combined with the era of big data and observation overlap opens up the possibility of discovering and analyzing large numbers of diverse SEBs, including those with high flux ratios and those in triple systems.

1. INTRODUCTION

The Apache Point Observatory Galactic Evolution Experiment (APOGEE) is studying our Galaxy in fantastic detail by providing high resolution spectra for some 150,000 stars (Majewski et al. 2015). Some of these belong to double-lined spectroscopic eclipsing binaries (SEBs), and a further subset have been observed by the *Kepler* spacecraft (Borucki et al. 2010) and appear in the *Kepler* Eclipsing Binary Catalog (Kirk et al. 2016). These APOGEE/*Kepler* SEBs which have several APOGEE spectra at different epochs give a unique opportunity to combine the spectra with the *Kepler* light curve to model the binary orbit and directly measure fundamental stellar parameters, including mass and radius. They can then be used to explore and constrain stellar evolution, stellar populations, and orbital kinematics.

While much work has gone into exploring *Kepler* eclipsing binaries (EBs) as a population, fewer studies have maximally utilized complementary spectra to

fully characterize these stellar systems. A notable exception is Matson et al. (2017), which found the radial velocities of 40 *Kepler* binaries, 35 of them double-lined and the remainder single-lined. Their work used medium resolution ground-based spectra, but the authors note that high resolution spectra is more optimal. In another example, Torres et al. (2018) used *K2* light curves of the Ruprecht 147 cluster together with high resolution spectra and the cluster's well-modeled metallicity to constrain the orbital parameters extracted from spectroscopic binary cluster members. In addition, Lehmann et al. (2012) analyzed the quadruple system KIC 4247791 by combining *Kepler* light curves and moderate resolution spectra.

Many studies have used APOGEE and *Kepler* data together, such as the APOKASC catalog (Pinsonneault et al. 2018, 2014) which combines APOGEE stellar parameters with *Kepler* asteroseismology. However, such works tend to ignore stellar multiplicity. The SEB overlap between APOGEE and *Kepler* in particular remains

relatively unexplored. There is also synergy with the *Kepler* planet survey which identifies candidate planet systems, some of which are found to be eclipsing binaries, with or without tertiaries, with follow-up radial-velocity observations with APOGEE (Fleming et al. 2015). The frequency of binaries, with and without tertiary companions, is a necessary component of computing transiting exoplanet astrophysical false-alarm probabilities (e.g. Morton et al. 2016).

EBs have long been used as fundamental benchmarks for stellar astrophysics (e.g., Torres et al. 2010), including more recently as benchmarks for exoplanet properties (e.g., Stassun et al. 2017), to test asteroseismic inferences of stellar parameters (e.g., Gaulme et al. 2016), and even for assessing trigonometric parallaxes (Stassun & Torres 2018). In addition, as they are often observed as SEBs, EBs are useful for assembling reliable statistics on the occurrence of higher order multiples (e.g., tertiary companions) and on the relationship of companion properties to the properties of the EB. For example, Tokovinin (1997) found the incidence of wide tertiaries to be strongly linked to the orbital period of the inner binary. Additional well-studied EBs can help to further test these relationships.

In this work, we identify 33 promising APOGEE/*Kepler* SEBs and compute full orbital solutions with a suite of stellar parameters for seven of them. In §2, we detail our sample selection, data processing, and modeling methodology. We further show how the Broadening Function technique is a superior method to extract multiple velocity components from APOGEE spectra. Subsequently §3 discusses each of the seven modeled systems in turn and presents orbital solutions. Finally, §4 places the SEBs in the context of each star’s stellar evolutionary history and explores the relationship of the EB orbital properties to the presence of tertiary companions.

2. DATA AND METHODS

2.1. Sample Selection

We use the following criteria and filters to arrive at a candidate sample of promising SEBs in the APOGEE/*Kepler* overlap. We begin with the *Kepler* EB catalog compiled by Kirk et al. (2016). From this catalog we select targets which have both their primary and secondary eclipses observed by *Kepler*; this limits our selection to binaries with inclinations close to 90 degrees. We further require the light curve to be semi- or well-detached, with the morphology parameter significantly less than 1. Next, a luminosity limit of $H < 14$ magnitudes was imposed, as fainter targets are unlikely to have H -band APOGEE spectra with a sufficiently

high signal-to-noise ratio. We also require the targets to have multiple cross-correlation function (CCF) peaks from the APOGEE pipeline (Nidever et al. 2015) visible by eye in one epoch. Finally, the binaries must have been observed by APOGEE at least three times, and thus have at least three `apVisit` spectra, with no quality flags present.

Taken together, these criteria result in 33 candidates, which are listed in Table 2, plus one additional candidate which has already been analyzed (Rawls et al. 2016). Of these, we perform a detailed analysis of seven. Notes in Table 2 indicate why we choose to exclude the other systems at this time. Several are being investigated by the *Kepler* APOGEE EB Working Group, some have only three APOGEE visits which would make a good RV curve solution challenging without additional spectra, some have low signal-to-noise (S/N) ratios, one shows significant ellipsoidal variations which are not included in our photometric model, and two remain good candidates for future analyses.

2.2. Radial Velocities (RVs) from APOGEE Spectra

The standard observing mode for APOGEE spectra has a total exposure time of roughly three hours, which is usually collected over a series of visits on different days. The visits are then combined into one spectrum per target (an `apStar` spectrum). We instead utilize individual visit spectra (`apVisit`), which are identified with their plate ID, date (MJD), and fiber ID. These may be retrieved from the SDSS Science Archive Server search tool with a simple search by APOGEE ID. We continuum normalize the visit spectra and then “de-spike” them to remove erroneous spectral features due to tellurics. De-spiking consists of identifying outliers above or below the continuum by 0.7 or 3 times the standard deviation of the normalized flux, respectively. The “below continuum” factor is larger to avoid unintentionally removing real absorption line features. Around each outlier spike, a $\pm 6 \text{ \AA}$ window is also flagged for removal. The python scripts used to retrieve, continuum normalize, and de-spike `apVisit` spectra are publicly available on GitHub¹. They rely heavily on the `apogee` python package on GitHub described in Bovy (2016).

In the main APOGEE reduction pipeline (Nidever et al. 2015), RVs are measured using the CCF. In this approach, a template spectrum and a series of visit spectra for a given target are cross-correlated, giving the RV of the target star relative to the template.

The CCF method works because an observed stellar spectrum can be represented as a convolution of two

¹ <https://github.com/mrawls/apVisitproc>

Table 2. Promising SEBs observed by APOGEE and Kepler, sorted by Kepler magnitude (K_p)

KIC	APOGEE ID	Visits	K_p	P_{orb} (day)	SE Depth (frac)	Morphology	Reference	Notes
9246715	2M20034832+4536148	2	10.08	171.28	0.1124	0.11	Rawls et al. (2016)	
2708156	2M19302686+4318185	3	10.67	1.89	0.0625	0.57		Only 3 visits
3120320	2M19291007+3817041	3	11.28	10.27	0.0127	0.14		Kepler APOGEE/EB WG
4851217	2M19432016+3957081	6	11.32	2.47	0.1815	0.58		Low S/N ratio
3439031	2M19203184+3830492	3	11.50	5.95	0.4156	0.33		Kepler APOGEE/EB WG
5285607	2M19390532+4027346	6	11.69	3.90	0.0403	0.36	This work	
6449358	2M19353513+4149543	25	11.72	5.78	0.0120	0.31	This work	
10206340	2M19245882+4714573	3	11.78	4.56	0.2431	0.61		Only 3 visits
6864859	2M19292405+4223363	25	11.93	40.88	0.2426	0.06	This work	
4931073	2M19351913+4001522	6	12.18	26.95	0.0564	0.08		Kepler APOGEE/EB WG
3127817	2M19355993+3813561	6	12.24	4.33	0.0512	0.48		Kepler APOGEE/EB WG
3335816	2M19184759+3824238	3	12.40	7.42	0.0106	0.16		Kepler APOGEE/EB WG
5284133	2M19373173+4027078	6	12.50	8.78	0.0492	0.15		Future work
3542573	2M19232622+3838017	3	12.61	6.94	0.0837	0.25		Only 3 visits
2711114	2M19240341+3758109	3	12.63	2.86	0.0022	0.29		Only 3 visits
4281895	2M19441242+3923418	6	12.76	9.54	0.0652	0.13		Only 3 visits
4660997	2M19340328+3942410	6	12.78	0.56	0.2527	0.62		Ellipsoidal variations
4473933	2M19363898+3933105	6	12.87	103.59	0.0126	0.25		Low S/N ratio
2305543	2M19280644+3736023	3	12.97	1.36	0.1052	0.50		Only 3 visits
3241619	2M19322278+3821405	3	13.06	1.70	0.1625	0.44		Only 3 visits
4285087	2M19463571+3919069	6	13.19	4.49	0.2408	0.31	This work	
2576692	2M19263432+3748513	3	13.19	87.88	0.2588	0.04		Kepler APOGEE/EB WG
6131659	2M19370697+4126128	27	13.20	17.53	0.1036	0.09	This work	
4847832	2M19401839+3957298	6	13.20	30.96	0.3200	0.08		Kepler APOGEE/EB WG
5025294	2M19414825+4010323	6	13.27	5.46	0.0010	0.18		Future work
6778289	2M19282456+4215080	25	13.31	30.13	0.1619	0.11	This work	
3248332	2M19383951+3819588	6	13.37	7.36	0.0974	0.20		Kepler APOGEE/EB WG
6610219	2M19320615+4200049	25	13.58	11.30	0.2899	0.20		Low S/N ratio
6781535	2M19321788+4216489	25	14.14	9.12	0.0305	0.12	This work	
4077442	2M19452193+3908260	6	14.35	0.69	0.0703	0.59		Kepler APOGEE/EB WG
3247294	2M19374558+3822510	6	14.35	67.42	0.1032	0.02		Kepler APOGEE/EB WG
3848919	2M19241352+3858278	3	14.48	1.05	0.3418	0.57		Low S/N ratio
5460835	2M19411125+4039416	6	14.72	21.54	0.0228	0.06		Low S/N ratio
4075064	2M19432862+3908535	6	15.71	61.42	0.0821	0.00		Low S/N ratio

functions: that of the astrophysical target (which includes “natural broadening” components such as thermal broadening, microturbulence effects, and instrumental broadening) and another function called the Broadening Function (BF) that contains the important RV information. The BF is formally presented in Rucinski (1992, 1999, 2002, 2004). Although the CCF method is very close to the real convolution that occurs in an APOGEE spectrum, cross-correlating a template spectrum with an observed stellar spectrum yields a function which inherits the natural broadening components present in both spectra. In this way the CCF is essentially a non-linear proxy of the BF. Therefore, instead of using the CCF, in this work we measure the BF directly.

To extract BFs from our target spectra, we use a modified version of the BF software suite from Rawls et al. (2016) which is based on the method introduced by Rucinski (1992). A PHOENIX BT-Settl model atmosphere spectrum (Husser et al. 2013) is selected to

match the target’s approximate spectral parameters as reported by APOGEE. The match cannot be exact as the two stars in a binary may not have identical spectral types and the model grid has a finite sampling in stellar parameters. In general, a mismatch in spectral type between template and target causes the BF to change in its intensity scale and quality, but the amplitudes of the RV components remain unchanged (Lu et al. 2001).

We examine the BF peaks by eye to identify their approximate locations on the radial velocity axis and use a least-squares fitting procedure to fit one or more Gaussians to the BF. The location of each Gaussian’s mean is the RV, which we then correct with the barycentric velocity provided with each `apVisit` spectrum. Our reported RV uncertainties come from the error in fitting a Gaussian to each BF peak using least-squares. Much like in the APOGEE CCF pipeline (Nidever et al. 2015), it is ultimately the uncertainty in the measurement of the BF peak, which depends partially on its semi-arbitrary

width, that determines the reported uncertainties for the RVs. This systematically underestimates the uncertainty of each RV measurement. The software used to extract RVs as described here is publicly available on GitHub.

In Figures 1 and 2, we demonstrate how the BF method produces significantly better separated peaks for APOGEE double-lined SEBs than the CCFs generated by the APOGEE pipeline. Due in part to the BF method having less of a “peak-pulling” effect, this more defined separation dramatically improves our ability to measure the RV of each component. We present the BF and measured RVs for each of our seven targets in Appendix A.

We also measure flux ratios in the APOGEE H band with our BF peaks, as the ratio of the peak areas is directly proportional to the flux ratio of the binary (Bayless & Orosz 2006; Stassun et al. 2007). These BF flux ratios will generally differ from *Kepler*-derived flux ratios because of the difference in wavelength; APOGEE is an H -band spectrograph and *Kepler* has a broad visible light bandpass. The BF flux ratios are discussed further in Section 3.8 alongside other variables for RV extraction and temperature estimation.

2.3. *Kepler* Light Curve Processing

We use minimally-processed *Kepler* long-cadence simple aperture photometry (SAP) to construct EB light curves for each target. Each light curve, and its uncertainties, is normalized by the median raw flux value of all available quarters. We de-weight data of poor quality by selecting times with *Kepler* quality flags > 0 , and inflating the normalized flux uncertainties at these times by a factor of 10.

2.4. *Orbital and Mass Solutions with KEBLAT*

With RVs in hand, we turn to the photometric modeling of the *Kepler* light curves. We utilize a modular Python tool dubbed “KEBLAT” which is capable of separate or simultaneous modeling of the binary light curve, spectral energy distribution (SED), and RV time series (Windemuth et al. 2018). Here, we simultaneously model *Kepler* light curves and APOGEE RVs of each EB in our sample to determine orbital solutions (P , e , ω , i , t_{PE}), stellar parameters (m_1 , m_2 , r_1 , r_2 , $\frac{F_2}{F_1}$), quadratic limb darkening coefficients under triangular reparameterization ($q_{1,1}$, $q_{1,2}$, $q_{2,1}$, $q_{2,2}$; Kipping 2013), and systemic radial velocity k_0 . For parameter sampling purposes, we transform individual mass and radius parameters to sums and ratios, and parameterize e and ω as $e \cos \omega$ and $e \sin \omega$.

Given a system’s total mass, period, eccentricity, argument of periastron, inclination, and time of primary

eclipse, KEBLAT uses a Keplerian solver to compute the instantaneous positions and velocities of each stellar component. The positions, along with specified sizes and relative flux of the stars are then used to determine the instantaneous light contribution during eclipse via a quadratic limb-darkening (Mandel & Agol 2002) model for spherical bodies.² We account for finite sampling effects (Kipping 2010) on the light curve by down-sampling 1-minute eclipse profiles to the *Kepler* long cadence ($dt = 0.0204$ d). Stellar and instrumental noise is marginalized by fitting the lowest non-linear order quadratic polynomial around each eclipse. We apply quarterly crowding values from *Kepler* to model third light contamination. To account for underestimated observational uncertainties and additional noise, we fit for a systematic light curve error $\sigma_{\text{sys,LC}}$, which we add in quadrature to the observed errors.

The z-component of the velocity, as solved by Kepler’s equation, is used to model the extracted RVs. For double-line eclipsing binary systems, where the RVs of both components are detected, the amplitudes of the primary and secondary RV are related to the masses of the secondary and primary, respectively. For single-line EBs, where only the RV of the brightest component is detected, only the “mass function” f_M of the system can be constrained, where

$$f_M = \frac{M_2^3 \sin^3 i}{(M_1 + M_2)^2}. \quad (1)$$

As with the light curve data, we fit for a systematic radial velocity error parameter $\sigma_{\text{sys,RV}}$ to account for underestimated noise.

We combine RVs with *Kepler* light curve information to model the system and find a best fit solution. We first determine the light curve and RV solutions separately, and then fit RV and light curve simultaneously. The simultaneous RV+LC model has 17 free parameters in total. The model is optimized via a least-squares algorithm `lmfit` (Newville et al. 2016), and then uses the best-fit solution to seed Monte Carlo Markov Chain (MCMC) simulations with `emcee` (Foreman-Mackey et al. 2013), in order to sample the posterior distributions of each parameter. We use broad, uniform priors and run the Markov chains with 128 walkers for $\sim 100,000$ iterations, visually inspecting trace plots for convergence. We report the 50%, 16%, and 86% values, i.e., the mean and 1σ uncertainties for each parameter. For more details on the KEBLAT model, including parameter bounds, see Windemuth et al. (2018).

² The assumption of spherical stars requires that the stars be sufficiently detached to avoid tidal and rotational distortions.

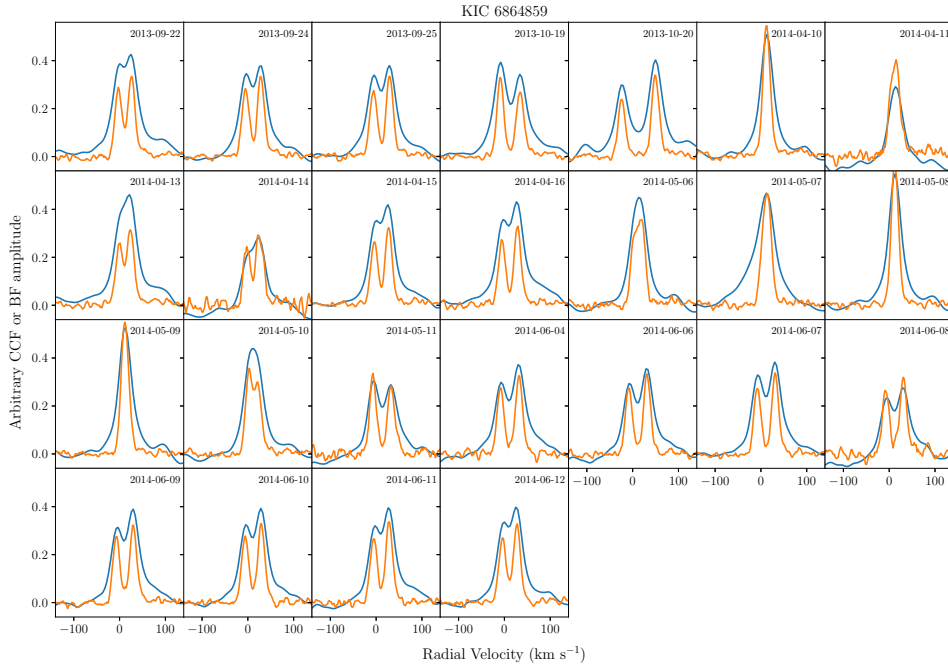


Figure 1. The BF (orange) is significantly better at resolving multiple velocity components from APOGEE visit spectra than the CCF (blue). This example shows visits for KIC 6864859. The y-axis amplitude is arbitrarily scaled for clarity. While it is clear from most of the CCFs that KIC 6864859 is a double-lined SEB, the BF more clearly separates the contribution from each star.

2.5. Radius ratio—flux ratio—inclination Degeneracy

For light curves with partially or grazing eclipsing geometries, there exists a degeneracy between radius ratio and flux ratio when eclipses are observed in a single photometric band. For this reason, we use additional constraints on the *Kepler* light curve flux ratios with spectroscopic *H*-band flux ratios obtained from the BF for SEBs exhibiting shallow eclipses (KIC 5285607 and KIC 6781535). For these two systems, we place a Gaussian prior on the RV+LC solution with μ centered around the BF-derived flux ratio and $\sigma = 0.2$.

2.6. Temperatures from Flux Ratios and Radii

Obtaining effective temperatures of the stars in these SEBs requires additional analysis. The KEPLAT model does not provide a measure of stellar temperatures directly, but only indirectly via the flux ratio in the *Kepler* bandpass. In addition, the APOGEE Stellar Parameter and Chemical Abundances Pipeline (ASPCAP) processing reports only a single “combined light” effective temperature for each system (Pérez et al. 2016). This ASPCAP temperature is likely to be biased due to the contamination of the brighter star’s spectrum by

the fainter star. Here we address both of these issues to estimate individual stellar effective temperatures.

The orbital solutions described in §2.4 yield sums and ratios of radii. In addition, the light curve analyses yield flux ratios ($F_{\text{ratio}} \equiv \frac{F_2}{F_1}$) in the *Kepler* bandpass which are primarily constrained by the observed eclipse depths.

By assuming the ASPCAP effective temperature is the flux weighted average of the system, $T_{\text{avg}} = (F_1 T_1 + F_2 T_2) / (F_1 + F_2)$, and defining the primary star as the one that provides the majority of the light, we can use the following relationships between the flux ratio F_{ratio} , T_{avg} , stellar radii R_1 and R_2 , and distance d to find flux and temperature estimates for the individual binary components separately. First, we solve for the binary’s flux sum using *Gaia* distance estimates from Bailer-Jones et al. (2018):

$$F_{\text{sum}} = \frac{\sigma T_{\text{avg}}^4 (R_1^2 + R_2^2)}{d^2}, \quad (2)$$

from which we can compute the individual fluxes as

$$F_1 = \frac{F_{\text{sum}}}{1 + F_{\text{ratio}}} \quad (3)$$

and

$$F_2 = F_{\text{sum}} - F_1. \quad (4)$$

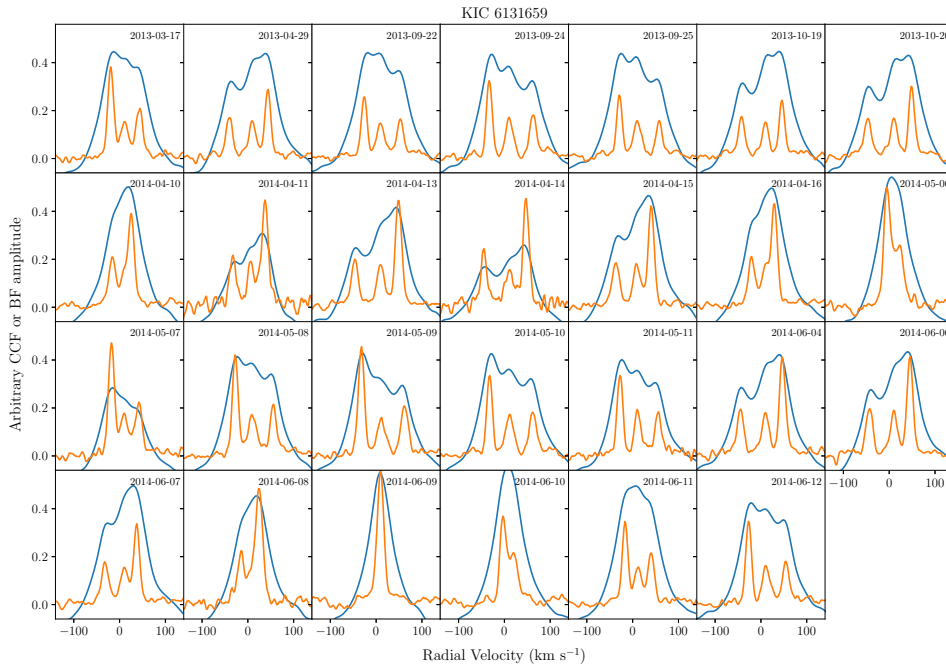


Figure 2. A second example, as in Figure 1, showing that the BF (orange) does a better job of resolving multiple velocity components than the CCF (blue). The y-axis amplitude is arbitrarily scaled for clarity. While it is clear from some of the CCFs that KIC 6131659 has more than one component, the three-component nature is immediately obvious in the BF. In all but a few cases, it is straightforward to precisely measure the RV of all three BF peaks. This is not true for any visit using the APOGEE CCFs.

Then, we use the relationship between T_{ave} , F_{ratio} , and the individual stellar fluxes to solve for the temperature of each star:

$$T_{\text{avg}} = T_2 \frac{F_{\text{ratio}}^{-1} T_{\text{ratio}}^{-1} + 1}{F_{\text{ratio}}^{-1} + 1}, \quad (5)$$

which yields

$$T_1 = \sqrt[4]{\frac{F_1 d^2}{\sigma R_1^2}} \quad (6)$$

and

$$T_2 = \sqrt[4]{\frac{F_2 d^2}{\sigma R_2^2}}. \quad (7)$$

However, these resulting temperature estimates are likely systematically underestimated. In the ASPCAP pipeline, APOGEE spectra are compared to a synthetic spectral model to resolve quantities like effective temperature. When a detached binary signature is present in stellar spectra, the additional component can cause the spectrum to be fit by a cooler synthetic template. This leads to a systematic underestimation in the binaries' effective temperatures of roughly 300 K (El-Badry

et al. 2017). The systematic underestimation is a function of the effective temperature of the primary and the mass ratio of the system. We follow their method for each system to correct for this effect.

3. RESULTS

The joint light curve and RV analysis for each of the seven systems is presented in detail in the following subsections. We present orbital and mass solutions together in Table 3.

In all systems, we define the primary eclipse ($\phi = 0$) as the deeper eclipse. This corresponds to when the primary star is eclipsed by the secondary star. Usually, the primary star is the brighter of the two, and the light curve definition of primary and the RV definition of primary agree. However, we note the secondary star in KIC 6781535 is brighter in the APOGEE H -band than the primary. In the figures that follow, we color code the RV of the primary star in red and the RV of the secondary star in orange.

Table 2. Binary Orbital and Stellar Parameters

	KIC 5285607 ^a	KIC 6864859	KIC 6778289	KIC 6449358	KIC 4285087	KIC 6131659	KIC 6781535 ^a
f_M	0.126 ^{+0.002} _{-0.002}
M_1 (M_\odot)	1.557 ^{+0.038} _{-0.033}	1.411 ^{+0.028} _{-0.022}	1.512 ^{+0.022} _{-0.022}	...	1.135 ^{+0.013} _{-0.014}	0.942 ^{+0.010} _{-0.010}	1.003 ^{+0.039} _{-0.038}
M_2 (M_\odot)	1.346 ^{+0.033} _{-0.033}	1.354 ^{+0.028} _{-0.028}	1.092 ^{+0.019} _{-0.018}	...	1.101 ^{+0.013} _{-0.014}	0.703 ^{+0.008} _{-0.008}	1.034 ^{+0.040} _{-0.040}
R_1 (R_\odot)	2.003 ^{+0.062} _{-0.054}	1.655 ^{+0.012} _{-0.013}	1.748 ^{+0.009} _{-0.009}	2.1254 ^{+0.0007} _{-0.0006}	1.033 ^{+0.010} _{-0.012}	0.908 ^{+0.003} _{-0.003}	1.199 ^{+0.113} _{-0.065}
R_2 (R_\odot)	1.679 ^{+0.063} _{-0.087}	1.455 ^{+0.012} _{-0.012}	0.998 ^{+0.005} _{-0.005}	0.6977 ^{+0.0005} _{-0.0004}	1.026 ^{+0.011} _{-0.011}	0.616 ^{+0.003} _{-0.003}	1.434 ^{+0.066} _{-0.114}
P_{orb} (d)	3.89940111 ^{+4.4e-8} _{-4.5e-8}	40.8778425 ^{+2.9e-7} _{-3.0e-7}	30.1301385 ^{+3.5e-7} _{-3.5e-7}	5.77679431 ^{+5.1e-8} _{-4.9e-8}	4.48603142 ^{+5.1e-8} _{-5.4e-8}	17.52782741 ^{+2.2e-7} _{-2.3e-7}	9.12208640 ^{+2.5e-7} _{-2.4e-7}
t_{pe} (d)	126.577647 ^{+1.1e-5} _{-9.7e-6}	158.3189733 ^{+9.2e-6} _{-7.6e-6}	122.100819 ^{+1.0e-5} _{-1.0e-5}	122.0739252 ^{+7.1e-6} _{-7.2e-6}	133.450881 ^{+1.1e-5} _{-1.1e-5}	127.042190 ^{+1.1e-5} _{-1.1e-5}	138.838193 ^{+4.8e-5} _{-6.6e-5}
i (rad)	1.3656 ^{+0.0015} _{-0.0009}	1.5415 ^{+0.0001} _{-0.0001}	1.55876 ^{+0.0001} _{-0.0001}	1.5327 ^{+0.0001} _{-0.0001}	1.5210 ^{+0.0001} _{-0.0001}	1.5558 ^{+0.0001} _{-0.0001}	1.4749 ^{+0.0007} _{-0.0004}
$e \sin \omega$	1.3e-6 ^{+9.0e-4} _{-1.2e-4}	-0.0254 ^{+0.0006} _{-0.0005}	-0.2337 ^{+0.0004} _{-0.0004}	0.00060 ^{+0.00046} _{-0.00040}	1.8e-4 ^{+1.4e-3} _{-3.0e-4}	-0.0127 ^{+0.0004} _{-0.0005}	0.0215 ^{+0.0034} _{-0.0026}
$e \cos \omega$	-8.6e-7 ^{+3.5e-6} _{-4.1e-6}	-0.634115 ^{+0.00001} _{-0.00001}	0.051090 ^{+0.000005} _{-0.000005}	-0.00023 ^{+1.0e-5} _{-1.1e-5}	-5.9e-5 ^{+3.7e-6} _{-3.8e-6}	7.1e-5 ^{+1.7e-6} _{-1.8e-6}	0.25005 ^{+0.00001} _{-0.00001}
F_2/F_1	0.6579 ^{+0.0959} _{-0.1025}	0.7256 ^{+0.0139} _{-0.0124}	0.19155 ^{+0.00002} _{-0.00002}	0.010752 ^{+6.5e-6} _{-6.5e-6}	0.9455 ^{+0.0396} _{-0.0356}	0.1480 ^{+0.0010} _{-0.0010}	1.0654 ^{+0.2195} _{-0.2384}
$q_{1,1}$	0.3690 ^{+0.0158} _{-0.0157}	0.4313 ^{+0.0158} _{-0.0146}	0.2930 ^{+0.0146} _{-0.0146}	0.3570 ^{+0.0082} _{-0.0099}	0.4632 ^{+0.0369} _{-0.0413}	0.1961 ^{+0.0042} _{-0.0039}	0.3786 ^{+0.0389} _{-0.0366}
$q_{1,2}$	0.0335 ^{+0.0407} _{-0.0242}	0.1113 ^{+0.0121} _{-0.0112}	0.3112 ^{+0.0179} _{-0.0169}	0.2961 ^{+0.0085} _{-0.0085}	0.3046 ^{+0.0518} _{-0.0460}	0.9959 ^{+0.0031} _{-0.0068}	0.7549 ^{+0.0938} _{-0.1037}
$q_{2,1}$	0.4027 ^{+0.0249} _{-0.0710}	0.3662 ^{+0.0269} _{-0.0259}	0.3991 ^{+0.0260} _{-0.0260}	0.3436 ^{+0.1530} _{-0.0509}	0.5470 ^{+0.0680} _{-0.0509}	0.0424 ^{+0.0076} _{-0.0070}	4056 ^{+0.0711} _{-0.0553}
$q_{2,2}$	0.0905 ^{+0.1343} _{-0.0579}	0.2377 ^{+0.0326} _{-0.0213}	0.3220 ^{+0.0329} _{-0.0306}	0.3189 ^{+0.3426} _{-0.2208}	0.2275 ^{+0.0427} _{-0.0381}	0.9380 ^{+0.0459} _{-0.0923}	0.2689 ^{+0.2181} _{-0.1750}
$M_1 + M_2$ (M_\odot)	2.903 ^{+0.068} _{-0.064}	2.765 ^{+0.052} _{-0.052}	2.604 ^{+0.038} _{-0.038}	...	2.236 ^{+0.025} _{-0.026}	1.645 ^{+0.017} _{-0.017}	2.040 ^{+0.073} _{-0.074}
M_2/M_1	0.863 ^{+0.014} _{-0.013}	0.960 ^{+0.015} _{-0.015}	0.723 ^{+0.009} _{-0.009}	...	0.969 ^{+0.007} _{-0.008}	0.746 ^{+0.005} _{-0.005}	1.030 ^{+0.026} _{-0.025}
$R_1 + R_2$ (R_\odot)	3.679 ^{+0.031} _{-0.033}	3.110 ^{+0.019} _{-0.020}	2.746 ^{+0.013} _{-0.013}	2.8231 ^{+0.0010} _{-0.0009}	2.060 ^{+0.008} _{-0.008}	1.525 ^{+0.005} _{-0.005}	2.632 ^{+0.034} _{-0.033}
R_2/R_1	0.839 ^{+0.055} _{-0.067}	0.879 ^{+0.008} _{-0.007}	0.5708 ^{+0.0003} _{-0.0003}	0.3283 ^{+0.0002} _{-0.0002}	0.993 ^{+0.020} _{-0.018}	0.679 ^{+0.003} _{-0.003}	1.222 ^{+0.113} _{-0.153}
b^d	1.5146 ^{+0.0473} _{-0.0576}	1.2407 ^{+0.0081} _{-0.0075}	0.3860 ^{+0.0005} _{-0.0005}	0.3413 ^{+0.0009} _{-0.0008}	0.7215 ^{+0.0079} _{-0.0076}	0.5533 ^{+0.0041} _{-0.0042}	1.9034 ^{+0.0960} _{-0.1341}
e	6.7e-5 ^{+9.6e-4} _{-6.2e-5}	0.63462 ^{+0.00001} _{-0.00001}	0.2392 ^{+0.0004} _{-0.0004}	0.00064 ^{+0.00045} _{-0.00033}	3.4e-4 ^{+1.3e-3} _{-2.6e-4}	0.0127 ^{+0.0005} _{-0.0004}	0.2510 ^{+0.0005} _{-0.0002}
$\ln(\sigma_{\text{LC, sys}})$	-8.76 ^{+0.01} _{-0.01}	-8.84 ^{+0.01} _{-0.01}	-8.48 ^{+0.01} _{-0.01}	-8.419 ^{+0.006} _{-0.006}	-6.81 ^{+0.01} _{-0.01}	-7.54 ^{+0.01} _{-0.01}	-8.12 ^{+0.01} _{-0.01}
k_0 (m s ⁻¹)	61668.8 ^{+532.1} _{-488.9}	93945.5 ^{+139.6} _{-142.6}	72332.2 ^{+213.8} _{-212.4}	68694.7 ^{+144.0} _{-147.0}	91275.4 ^{+248.5} _{-256.1}	89867.7 ^{+127.1} _{-125.2}	44547.4 ^{+633.7} _{-627.5}
$\ln(\sigma_{\text{RV, sys}} \text{ (m s}^{-1}\text{)})$	7.40 ^{+0.26} _{-0.23}	6.54 ^{+0.14} _{-0.13}	7.04 ^{+0.12} _{-0.11}	6.27 ^{+0.23} _{-0.20}	6.65 ^{+0.29} _{-0.23}	6.82 ^{+0.10} _{-0.10}	8.28 ^{+0.12} _{-0.11}

^a Broad Gaussian prior on flux ratio used based on BF results ($\sigma = 20\%$ BF value).

^b f_M is the mass function as defined in §2.4; instead of fitting directly for M_1 and M_2 , we used f_M for KIC 6449358 because it is a single-lined spectroscopic binary.

^c The fit zero-point for the time of primary eclipse is in units of BJJD (BJD - 2454833). The primary eclipse is defined here as the deeper of the two. This differs from the KEBC (Kirk et al. 2016) primary eclipse definition for KIC 6864859 only because the two eclipses have very similar depths.

^d The impact parameter b is defined as $a \cos i/R_1$, where q_1^1, q_2^1 and q_1^2, q_2^2 are triangularized quadratic limb darkening coefficients for star 1 and star 2 (see Section 2.4 for details). We use natural log for the systematic LC and RV error terms for fitting flexibility.

3.1. KIC 5285607

KIC 5285607 is a grazing ($i = 79^\circ$) 3.9 d eclipsing binary with similar mass stellar components ($M_1 = 1.56 M_\odot, M_2 = 1.35 M_\odot$). The stars are in a circular orbit, as exhibited by the sinusoidal shape of the RV and occurrence of secondary eclipse at a phase of ~ 0.5 as seen in Figure 3.

Because the eclipses in the light curves are shallow (4% loss of light), the impact parameter is highly degenerate with the flux and radius ratio. That is, a solution with similar flux contributions from both components in a more inclined system yields the same shallow eclipses as a solution with a much brighter primary component in a more edge-on system. This degeneracy can be ameliorated with additional information from spectra. Therefore, we place a Gaussian prior on the flux ratio parameter based on the BF fits, with a 0.2σ width. With this flux ratio constraint, we find the secondary star is about 80% the size of the primary, with absolute dimensions of $2.0 R_\odot$ and $1.7 R_\odot$ for the primary and secondary components, respectively.

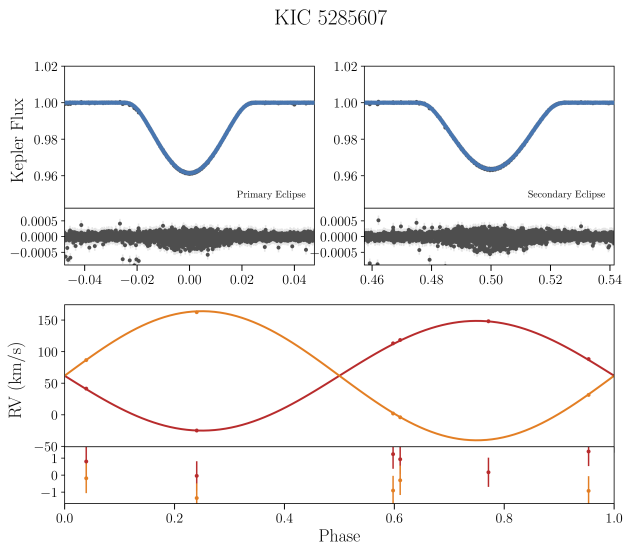


Figure 3. Simultaneous light curve (top panels) and radial velocity (bottom panel) fits to *Kepler* and APOGEE observations for KIC 5285607. The light curve data and residuals are shown in dark grey, with the model overlaid in blue. Note the shallow and V-shaped primary and secondary eclipses, which indicate a grazing system. The phased RV panel shows the BF derived values (points) and corresponding model (lines), where the primary RV is red and secondary RV is orange. The RV semi-amplitude is ~ 100 km/s while the residual scatter is ~ 1 km s $^{-1}$.

3.2. KIC 6864859

KIC 6864859 is a highly eccentric ($e \sim 0.6$), slightly inclined ($i = 88.32^\circ$) 40.9 d eclipsing binary with components of similar mass ($M_1 = 1.41 M_\odot, M_2 = 1.35 M_\odot$) and radii ($R_1 = 1.66 R_\odot, R_2 = 1.46 R_\odot$). The best-fit model is shown in Figure 4. The system’s highly eccentric orbit gives rise to irregularly shaped RVs and a secondary eclipse near phase ~ 0.125 .

Figure 5 shows clear brightening events of the system between primary and secondary eclipses, with maximal amplitudes ~ 0.3 ppt at phase ~ 0.065 , the predicted phase of periastron passage from KEBLAT. This behaviour is consistent with tidal distortions in an eccentric orbit near periastron, and is symptomatic of a class of objects known as “heartbeat” stars (Thompson et al. 2012). Both primary and secondary eclipse residuals exhibit small amplitude (~ 0.5 ppt) coherent structures; these are likely due to the non-spherical shape of the stars which is not explicitly modeled in KEBLAT.

We note that in our reduction process, some *apVisit* spectra were eliminated due to a very low signal-to-noise ratio that persisted after being run through our de-spike program. The majority of the remaining visits for this target resulted in well-separated peaks from the BF.

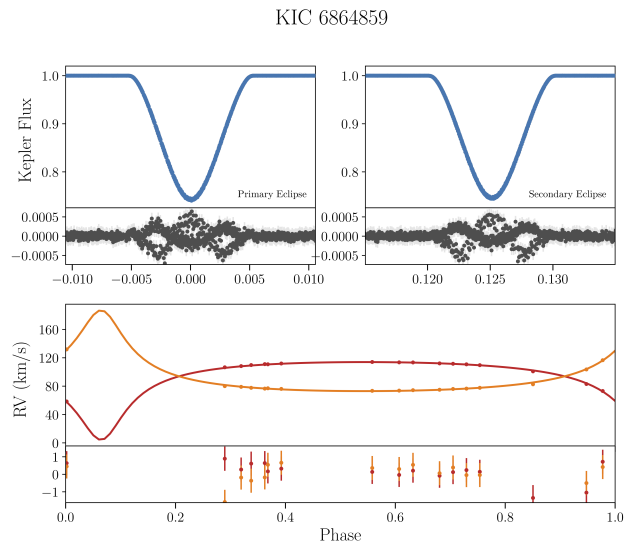


Figure 4. Simultaneous light curve (top panels) and radial velocity (bottom panel) fits to *Kepler* and APOGEE observations of KIC 6864859. The primary and secondary eclipses are similar in shape and depth with $\sim 25\%$ loss of light; the phase of secondary eclipse and shapes of the RVs indicate an extremely eccentric system. The light curve residuals are small but have a coherent shape, likely due to tidal and rotational distortion of the stars.

3.3. KIC 6778289

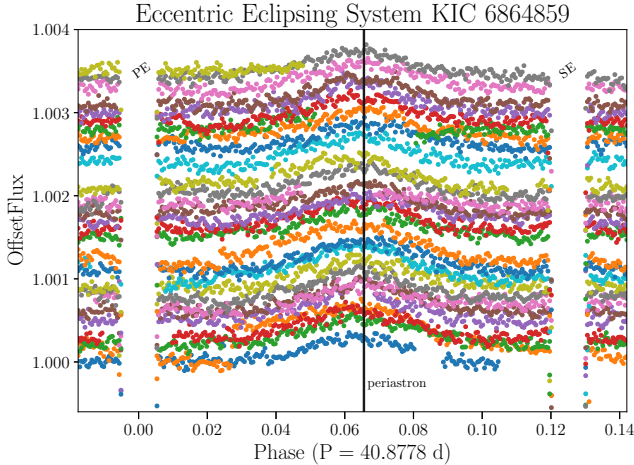


Figure 5. “Heartbeat” signatures of the eccentric eclipsing system KIC 6864659. The light curve surrounding primary and secondary eclipses is folded in phase and offset vertically between each observed orbit, using different colors for visual clarity. The brightening between primary and secondary eclipse is readily apparent around phase 0.065.

KIC 6778289 is a 30.1 d eclipsing binary with stellar components $M_1 = 1.51 M_\odot$ and $M_2 = 1.09 M_\odot$ in an eccentric ($e = 0.2$), nearly edge-on ($i = 89.3^\circ$) orbit. The simultaneous RV+LC fit is shown in Figure 6. The radii are $R_1 = 1.75 R_\odot$ and $R_2 = 1.0 R_\odot$. This difference in radius gives rise to the difference in primary and secondary eclipse shape. The flat-bottomed secondary eclipse indicates a total eclipse of the secondary component, while the primary eclipse is more V-shaped, e.g., more grazing. The larger residuals during secondary eclipse is consistent with starspot modulation. The system has low ($\approx 1\%$) third light contamination in the *Kepler* light curve which does not appear in the BF.

3.4. KIC 6449358

KIC 6449358 is a 5.8 d circular EB which may be a gravitationally bound to a distant tertiary companion.

The BF for this object exhibits two clear peaks, however, the second-brightest peak is relatively stationary in RV while the brighter peak varies by ~ 60 km/s over one orbit. This is shown in Figure 7 as well as in Appendix A Figure 19. If the \sim stationary BF peak corresponded to a stellar binary component, it would require a system with extremely large mass ratio $M_2/M_1 > 10$, which would be consistent with a white dwarf. However, the light curve constrains the radius ratio to be $R_2/R_1 \sim 0.3$, which makes this scenario physically implausible.

A more likely explanation for the \sim stationary RV component is that it belongs to a tertiary star, and that the true secondary stellar component of the EB is too

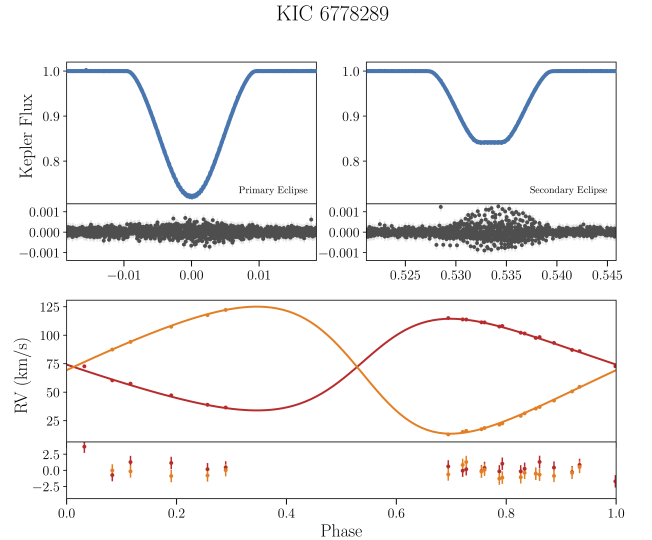


Figure 6. Simultaneous light curve (top panels) and radial velocity (bottom panel) fits to *Kepler* and APOGEE data for KIC 6778289. Different eclipse depths along with a flat-bottomed secondary eclipse indicate a smaller and dimmer secondary. Additionally, the unequal amplitudes and shape of the RV indicates an unequal mass binary with significant orbital eccentricity.

faint to be robustly detected by APOGEE. Indeed, the flux ratio in the *Kepler* bandpass is $F_2/F_1 \sim 0.01$. Thus, we effectively treat KIC 6449358 as a single-lined SEB in our model, and as a result we are only able to constrain the mass function f_M of the binary. Specifically, to reproduce the observed RV amplitude, our sum and ratio of masses solutions are degenerate, tending toward two extremes: high total mass ($\sim 4 M_\odot$) with a low mass ratio ($q \sim 0.3$), or low total mass ($1 M_\odot$) with a higher mass ratio ($q \sim 0.67$).

We note that some APOGEE visits do suggest a small, third BF peak (see Appendix A Figure 20 for details). These marginal BF peaks have large radial velocity variations from visit to visit, consistent with a low-mass star. This supports the scenario with total mass $\sim 2.3 M_\odot$ and mass ratio $q \sim 0.45$.

Figure 7 shows the best KEBLAT model fit to the light curve and radial velocities obtained using mass function $f_M = \frac{M_2^3 \sin i}{(M_1 + M_2)^2}$ her than M_1 and M_2 . The \sim stationary RV points, which are not fit, correspond to the putative third star, either a line-of-sight coincident or a tertiary companion in a hierarchical triple system. We favour the latter scenario, as the eclipses show timing variations consistent with perturbations by a bound, tertiary component. These eclipse timing variations (ETVs) have been used to identify and characterize many *Kepler* EBs (e.g. Borkovits et al. 2016), and we fit these ETVs using

a simple linear ephemeris based on the observed times of primary eclipse. We then compute the observed minus computed ($O - C$) eclipse times as a function of time. The result is shown in Figure 8. There is a clear parabolic or sinusoidal trend in the ETVs with an amplitude of ~ 0.0006 d; the ETV timescale indicates that the perturbing tertiary body has a minimum period ~ 1450 d. The architecture of this type of hierarchical triple – short, circular inner binary orbited by a distance tertiary companion – is consistent with dynamical processing via the Kozai (1962) mechanism.

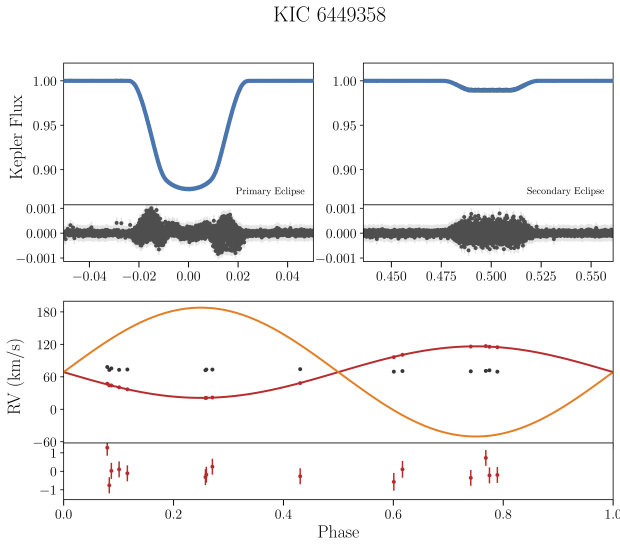


Figure 7. Simultaneous RV+LC fit for KIC 6449358, a single-lined spectroscopic binary suspected in a hierarchical triple system. We utilize mass function here than individual component masses to obtain the RV fit. The \sim stationary RV points near ~ 80 km/s are measured RVs of a tertiary companion, while the orange curve shown here is the predicted radial velocity of the unseen secondary, based on the locations of tentative BF peaks in Appendix A Figure 20. The flat-bottom secondary eclipse indicates the system is close to edge-on with a radius ratio ~ 0.33 , breaking the inclination-radius ratio degeneracy. The primary eclipse residuals are significant during ingress and egress, consistent with eclipse timing variations due to a tertiary companion (see Figure 8).

3.5. KIC 4285087

KIC 4285087 is an equal mass binary ($M_1 \approx M_2 \approx 1.1M_\odot$) in a circular, slightly inclined ($i = 87.3^\circ$) 4.5 d orbit. We show the best-fit solution in Figure 9. The components are main-sequence dwarfs with similar radii ($R_1 \sim R_2 \sim 1R_\odot$). The eclipses are similar depth ($\sim 30\%$), duration (~ 0.2 d), and shape (V), consistent with equal mass dwarfs orbiting each other.

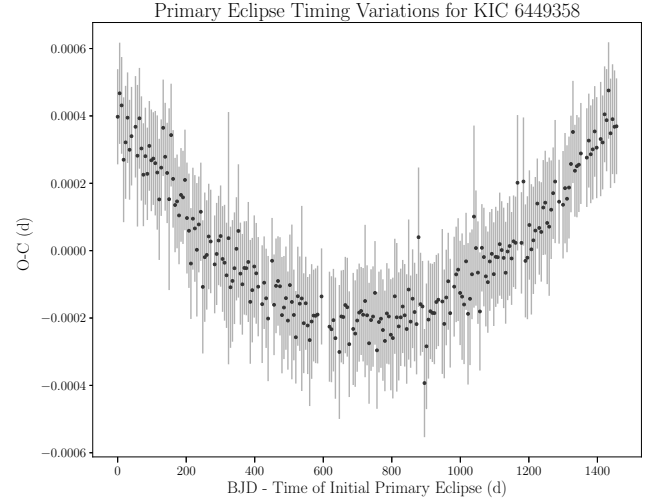


Figure 8. O-C diagram for KIC 6449358, showing primary eclipse timing variations; the ETVs exhibit a half-sinusoid trend, giving a rough estimate for the minimum period of the tertiary perturber to be $P \sim 1450$ d.

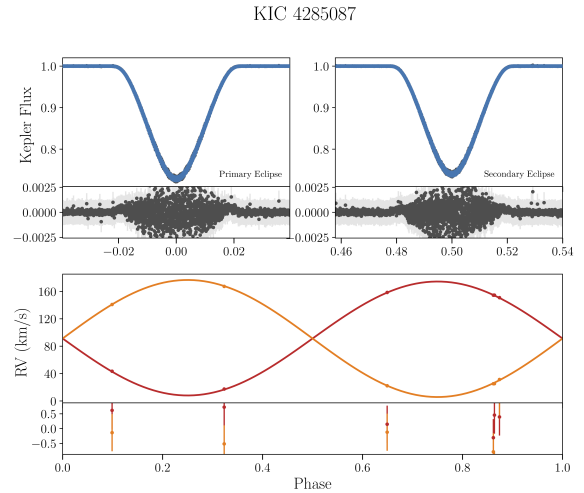


Figure 9. Simultaneous light curve (top panels) and radial velocity (bottom panel) fits to *Kepler* and APOGEE observations. The phase of secondary eclipse and shape of RVs indicate EBs in a \sim circular orbit. The light curve residuals during eclipse suggest the presence of a variable third light contribution, or non-Keplerian photometric effects given its short period. (~ 4 d).

3.6. KIC 6131659

KIC 6131659 is a mass ratio of 0.75 binary ($M_1 = 0.9 M_\odot$, $M_2 = 0.7 M_\odot$) in a 17.5 d, close-to-circular orbit. Figure 10 shows the simultaneous RV+LC fit to the data. The primary and secondary eclipses are relatively

deep, with 35% and 10% loss of total system light, respectively. The residuals to the light curve fit show correlated structure, which may be due to poor limb darkening modeling and/or a varying third light component which deviates from *Kepler* crowding values.

There is a third light component readily visible in the BF (see Appendix A Figure 22), but it is not RV-variable. This suggests it may be a line-of-sight contamination source or a gravitationally bound body in a hierarchical triple with an orbital period much longer than 17.5 d. The light curve does not show apparent eclipse timing variations, but this does not preclude the presence of a gravitationally bound tertiary.

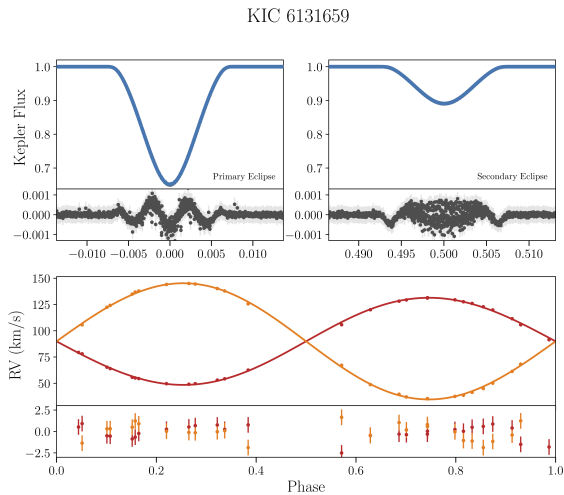


Figure 10. Simultaneous light curve (top panels) and radial velocity (bottom panel) fits to *Kepler* and APOGEE observations for KIC 6131659. The primary and secondary eclipses are relatively deep, with 35% and 10% loss of total system light, respectively.

3.7. KIC 6781535

KIC 6781535 is an eccentric ($e = 0.25$), grazing ($i = 84^\circ$), 9.1 d binary. The best-fit solution (see Figure 11) yields binary components of similar mass ($M_2/M_1 \approx 1.0$) but slightly different radii ($R_2/R_1 \approx 1.2 \pm 0.1$), which suggests a slightly evolved system. The shallow eclipses poorly constrain the system’s impact parameter, flux ratio, and radius ratio. As a result of this degeneracy, we apply a Gaussian prior on the light curve flux ratio parameter from spectra, following the same method as used for KIC 5285607 (see §3.1).

Similarly to KIC 6131659, there is a third light component visible in the BF (see Figure 23) that is not RV variable, indicating either a line-of-sight coincident third star or gravitationally bound tertiary companion. There

are symmetric structures in the light curve residuals, most noticeably during primary eclipse, consistent with variable third light contribution, changes to the binary orbit due to additional bodies, or starspot modulations. Because the system exhibits shallow, grazing eclipses, it was not conducive to an ETV analysis.

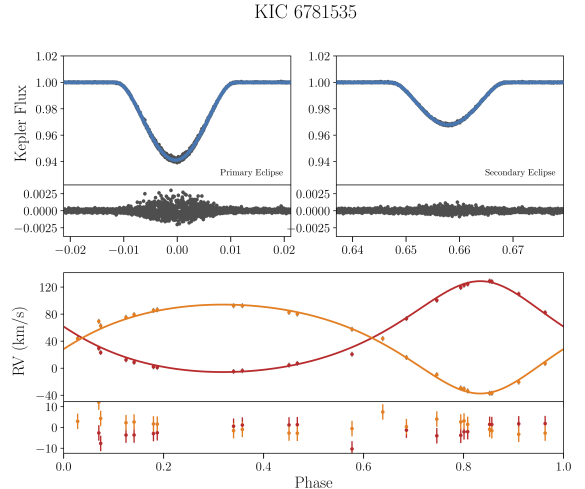


Figure 11. Top panels show the light curve model (blue) for KIC 6781535 overlaid against data (grey) as a function of phase. Bottom panel shows the RV model (lines) for primary (red) and secondary (orange) components overlaid on top of APOGEE-extracted data (points). The models correspond to the best-fit joint LC+RV solution.

3.8. Supplemental Physical Parameters

In addition to the main results in Table 3, we report some additional physical parameters in Table 3. As discussed in Section 2.6, we can use the BF peak area ratios to measure the *H*-band flux ratio of each system. We can also combine *Gaia* parallax information with our measured fluxes, radii, and the ASPCAP T_{eff} to estimate individual stellar temperatures. These parameters, along with adopted values from external sources, are summarized in Table 3.

4. DISCUSSION

4.1. Evolutionary Histories

With such well-characterized stars, we can investigate each binary’s age and evolutionary history with two different approaches. In the following we assume normal Milky Way metallicities $-0.5 < [M/H] < 0$.

First we explore the H-R diagram in $\log g$ vs. $\log T_{\text{eff}}$ after first correcting our temperature estimates following El-Badry et al. (2017). We calculate $\log g$ for each star directly from the KEBLAT mass and radius. We also

Table 3. Parameters related to RV extraction and temperature estimates

	KIC 5285607	KIC 6864859	KIC 6778289	KIC 6449358	KIC 4285087	KIC 6131659	KIC 6781535
BF Flux Ratio (F_2/F_1)	0.620 ± 0.027	0.811 ± 0.028	0.462 ± 0.029	0.392 ± 0.014	0.997 ± 0.023	0.648 ± 0.028	1.253 ± 0.115
ASPCAP T_{eff} (K) ^a	6495 ± 156	6417 ± 159	6572 ± 162	6237 ± 179	5664 ± 146	4845 ± 98	5749 ± 125
Gaia parallax (mas) ^b	1.254 ± 0.0216	1.4897 ± 0.0241	0.9093 ± 0.0222	1.1974 ± 0.0264	1.619 ± 0.0312	-0.5117 ± 1.0713	...
Gaia distance (pc) ^b	799 ± 14	671 ± 11	1100 ± 27	835 ± 18	617 ± 12
$\log g_1$ (cgs) ^c	4.028 ± 0.013	4.150 ± 0.010	4.133 ± 0.008	...	4.454 ± 0.006	4.496 ± 0.005	4.161 ± 0.019
$\log g_2$ (cgs) ^c	4.118 ± 0.015	4.244 ± 0.012	4.479 ± 0.010	...	4.478 ± 0.007	4.705 ± 0.006	4.253 ± 0.021
T_{eff} offset (K) ^d	350	80	250	...	20	350	100
Adopted $T_{\text{eff},1}$ (K)	6845 ± 328	6497 ± 159	6822 ± 162	6737 ± 178	5689 ± 146	5195 ± 98	5849 ± 125
Adopted $T_{\text{eff},2}$ (K)	6716 ± 293	6541 ± 283	7265 ± 440	8788 ± 658	5735 ± 105

^aDR14 (Pérez et al. 2016)^bBailer-Jones et al. (2018)^cComputed directly from M and R as reported in Table 3.^dEl-Badry et al. (2017)

use the KEBLAT masses and radii to determine the system ages in the mass-radius space directly, which avoids any dependence on distance or on our disentangling of the individual component temperatures.

In both approaches, we use Dartmouth evolutionary tracks (Dotter et al. 2008) and consider only the portion of the track with $\log g \geq 4.1$. This effectively only includes the main sequence. For consistency, we adhere to the KEBLAT definition of star 1 (primary) and star 2 (secondary) in which star 1 is the member of the SEB being eclipsed during the primary eclipsing event, and star 2 (secondary) as the member eclipsed during the secondary eclipsing event.

Figure 12 shows all of the SEBs in the $\log g$ vs. $\log T_{\text{eff}}$ diagram, and Figure 13 shows each SEB system individually. In general, the systems are broadly consistent with ages ranging from about 0.8 to about 3 Gyr, and the two components of each system appear to be consistent with a common age. Figure 14 represents these systems in the mass-radius diagram, where again all six systems modeled appear consistent with coevality for the same range of ages as above.

4.2. Mass-Luminosity Relationships

In order to verify that our targets are on the main sequence, we create a mass-luminosity plot (Figure 15) using the stellar masses from Table 3 and calculated H -band luminosities explained below. These luminosities are independent of the ASPCAP temperature estimates and corrections from El-Badry et al. (2017) used to derive Figures 13 and 14. The results represent a

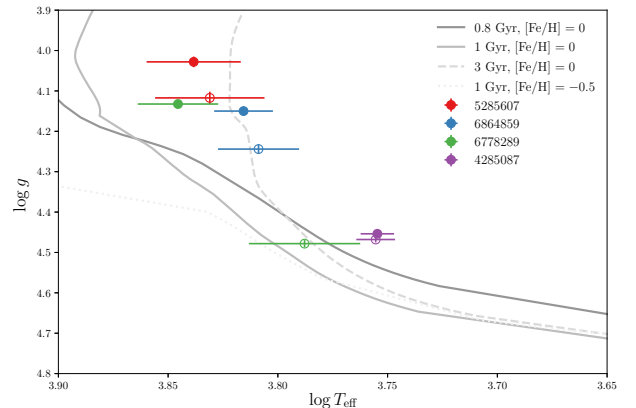


Figure 12. Spectroscopic H-R diagram for the systems with *Gaia* distances. Primaries are depicted with the solid circles while secondaries are open circles. A variety of Dartmouth isochrones are plotted with a range of ages 0.8–3 Gyr and metallicities (sub-solar to solar). Only the four targets with *Gaia* parallaxes are plotted here. Assuming Milky Way metallicity, we find all of our systems exhibit a high degree of coevality with ages ranging from 1–3 Gyr.

comparison to theoretical models that complements the mass-radius relationship presented in Figure 14, and is less reliant on light curve modeling, which may have degenerate radius solutions in grazing geometries.

To calculate H -band luminosities, we use distances derived from *Gaia* parallaxes (Bailer-Jones et al. 2018) to convert apparent H -band magnitudes from 2MASS (Skrutskie et al. 2006) to absolute magnitudes. We

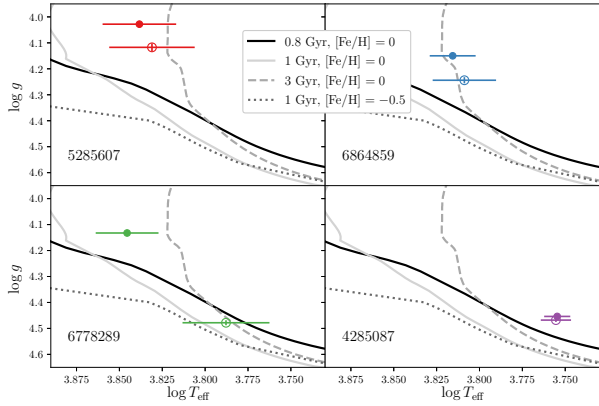


Figure 13. Figure 12, showing each SEB system individually. The filled circles model the primary star of the SEB, and the hollow circles the secondaries.

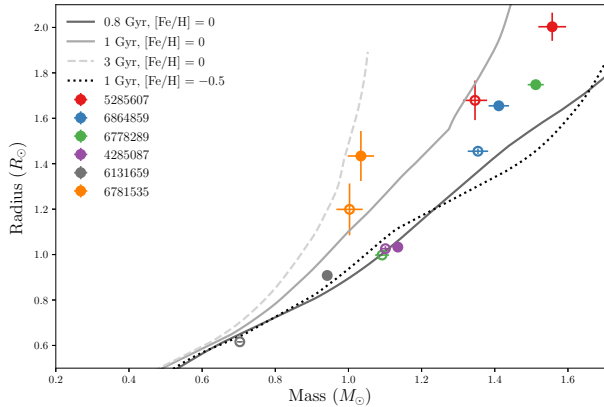


Figure 14. Radius versus mass diagram for all seven systems. Primaries are shown as solid circles and secondaries in open circles. Dartmouth isochrones for a variety of ages and metallicities are also plotted. All seven systems are consistent with coevality, ranging in age from about 1 to about 3 Gyr, assuming a normal Milky Way metallicity of $[M/H] = -0.5$

check that the H -band magnitudes were not taken during eclipse by cross referencing the time of 2MASS observations to the EB ephemeris. We then compute the system H -band luminosities from absolute magnitudes using the sun as a reference, with H -band magnitude of 3.32 from Cohen et al. (2003). We disentangle the separate luminosities for each stellar component in the system using the observed APOGEE H -band flux ratios (see Table 3). In Figure 15, we show each system using the same plotting convention as Figures 12 to 14, where solid and open circles correspond to primary and

secondary components, respectively. We over-plot for comparison theoretical masses and H -band magnitudes from Dartmouth isochrones (Dotter et al. 2008) at sub-solar and solar metallicity and a range of ages (0.8–5 Gyr). In general, as previously concluded, members of the same binary system follow the same evolutionary track, i.e., are coeval.

We exclude KIC 6449398 from this analysis, because it is a single-lined SEB. We also exclude KICs 6131659 and 6781535, which have negative parallax values from *Gaia*. For this reason we could not include these targets in the spectroscopic H-R diagram for our systems with *Gaia* distances. We did not include reddening corrections to the distance modulus calculations; however, reddening effects should be minimal in the near-IR (2MASS and APOGEE H -band) compared to the visible (*Kepler*).

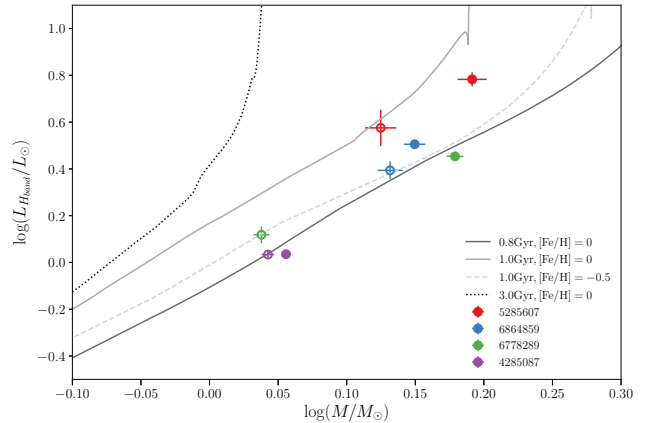


Figure 15. Mass-luminosity relationship for the four targets with accurate *Gaia* distances and RV-derived masses. Primaries are shown in solid circles and secondaries in open circles. Dartmouth isochrones (Dotter et al. 2008) are over-plotted as grey lines, corresponding to a variety of ages and metallicities.

4.3. Tertiary Companions

In our subset of SEBs, we identified three candidate triple systems. The binaries with possible tertiary companions are KIC 6131659, KIC 6781535, and KIC 6449358 (see Sections 3.6, 3.7, and 3.4, respectively). The first two of these systems exhibit clear third BF component peaks in nearly all RV visits. We fit these third peaks with Gaussians, similar to the Gaussian fits for the primary and secondary BF components. In both cases, the third BF components do not have radial velocity variations above the noise, which suggest these third members are either line-of-sight contamination sources

or gravitationally bound in hierarchical triples with orbital periods much longer than that of the observed SEB.

While statistics on multiplicity are not complete, numerous studies have found tertiary systems composed of a tight binary orbited by a distant third member. Statistics from Tokovinin et al. (2006) indicate that roughly 63% of spectroscopic binaries have tertiary companions in a wide orbit. In binaries with shorter periods (less than 3 days) this percentage rises to 96%, but in longer period binaries (12 or more days) this percentage is only 34%.

The incidence of triples among *Kepler* close eclipsing binaries (as are the ones in our analysis) is at least $\sim 20\%$ (Rappaport et al. 2013; Conroy et al. 2014), and likely higher for tertiaries with longer periods beyond *Kepler*'s finite observing time.

Evidence from both spectroscopic and photometric observations indicate KIC 6449358 belongs to a hierarchical triple system (see §3.4). The BF for this system shows a stationary tertiary peak in a few of the APOGEE visits. The mid times of eclipses in the *Kepler* light curve also exhibit sinusoidal variations in time; these eclipse timing variations indicate that the tertiary has a period $\gtrsim 1450$ d.

Interestingly, among our sample we do not detect tertiary companions among the shortest-period binaries. In particular, neither of the two EBs with $P_{\text{orb}} < 5$ d exhibits a clear tertiary in our data. It is not yet clear whether existing observations might already exclude the presence of tertiaries at very large separations that might not appear in our data; additional imaging observations might be required to identify such stars. At the same time, two of the four EBs with $P_{\text{orb}} > 9$ d are triples, which would appear to be an over-abundance of tertiaries among the longest-period EBs, albeit with a small sample. However, we note that one of these (KIC 6781535, $P_{\text{orb}} \approx 9$ d) is a modestly evolved system (see Figure 14), and excluding that case yields an occurrence of 1/3 triples among our EBs with $P_{\text{orb}} > 12$ d), fully consistent with the results of Tokovinin et al. (2006).

5. SUMMARY

We thoroughly characterize seven SEBs that have been observed by both *Kepler* and APOGEE. Our targets are selected from the *Kepler* EB catalog, and limited to bright, detached EB targets with both primary and secondary eclipses observed by *Kepler*, high inclination, and multiple APOGEE visits. We identify an additional 26 SEBs which may warrant similar studies. We demonstrate that the BF is a superior method for extracting RVs from APOGEE visit spectra compared to the CCF used in the present reduction pipeline. This

is particularly true for systems with multiple RV variable components. While such an analysis is beyond the scope of this work, if the BF method were applied to the full data set of multiple-visit APOGEE targets, it would most likely reveal many previously unknown SEBs and other interesting RV-variable sources.

RVs are extracted from *apVisit* spectra using the BF method and the *Kepler* light curves are normalized, de-weighted and modeled using KEBLAT. The light curve and RV solutions are first determined individually, and then computed simultaneously. We use the resulting physical parameters to estimate stellar temperatures, investigate coequality, and explore candidate triple systems.

Using our analysis we find our target's binary members are coeval with ages ranging from 1 to 3 Gyr, assuming normal Milky Way metallicity ($-0.5 < [M/H] < 0$). The exception is KIC 6781535 which lies closer to a slightly metal poor ($[M/H] \sim -1.0$) 3 Gyr isochrone. Our systems being broadly consistent with coequality confirms a common assumption in star formation that members of multiples form at the same time, and also effectively calibrates stellar evolution modeling.

Overlap between large scale surveys like APOGEE, *Kepler*, and *Gaia* allows us to discover and analyze many diverse SEBs, including systems with very low flux ratios and those in higher order systems. The statistics on the triples within our subset with respect to the orbital period of inner binaries is broadly consistent with statistics from the field Tokovinin (1997), though there may be some tension with our sample in that the shortest-period EBs do not appear to be spectroscopic triples. This is in contrast to the expectation that shortest-period EBs are most likely to be hierarchical triples. It is possible that very wide tertiaries do exist in these systems but have yet to be identified via imaging.

We have shown that through tools like KEBLAT and the BF analysis of APOGEE spectra, it is possible to perform high quality analysis of large numbers of SEBs with a variety of properties. This opens up great promise for future SEBs identified in TESS and SDSS-V data.

ACKNOWLEDGMENTS

We would like to thank Scott Fleming for critical guidance and discussion and Paul A. Mason for valuable brainstorming and advice. We recognize the SDSS Faculty And Student Team (FAST) initiative for supporting this work through a partnership with New Mexico State University. JMCC thanks the Fisk-Vanderbilt Masters-to-PhD Bridge Program, Amanda Cobb, Kelly Holley-Bockelmann, and Nancy Chanover for continued empowerment of a woman and new mother in STEM. MLR celebrates that this work has encompassed two births, one wedding, and multiple graduations among the lead authors.

Software: Astropy (Astropy Collaboration et al. 2013; Price-Whelan et al. 2018), PyAstronomy (Czesla

2018), Matplotlib (Hunter 2007), Apogee (Bovy 2016), Makecrite (Price-Whelan et al. 2018), Numpy (Van Der Walt et al. 2011), Pandas (McKinney 2010), Emcee (Foreman-Mackey et al. 2013), Gaussfitter (Ginsburg 2017), Scipy (Jones et al. 2001)

APPENDIX

A. STELLAR RADIAL VELOCITIES

Here, we include one Broadening Function plot for each of the seen targets. These illustrate how we measured radial velocities for each component of the spectroscopic binaries from APOGEE visit spectra, as discussed in Section 2.2. Note each figure uses uncorrected RV on the abscissa, before barycentric corrections have been applied. The final corrected RVs with uncertainties are reported in Table 3 below.

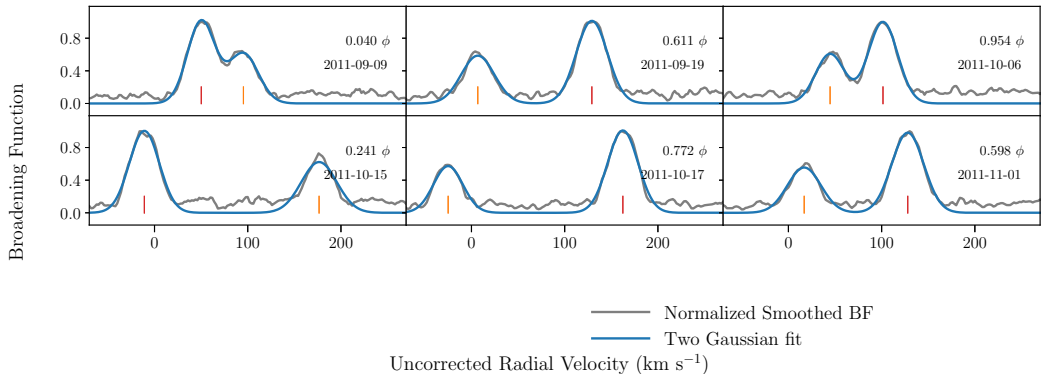


Figure 16. BF plots for KIC 5285607. The normalized smoothed BF is shown in grey while the Gaussian fits are modeled in blue. Uncorrected radial velocities are shown on the abscissa in km s^{-1} , and arbitrary amplitude of the BF on the vertical axis. In this case the primary (red) is distinguishable from the secondary (orange), and the visit spectra were well separated over the course of the observations.

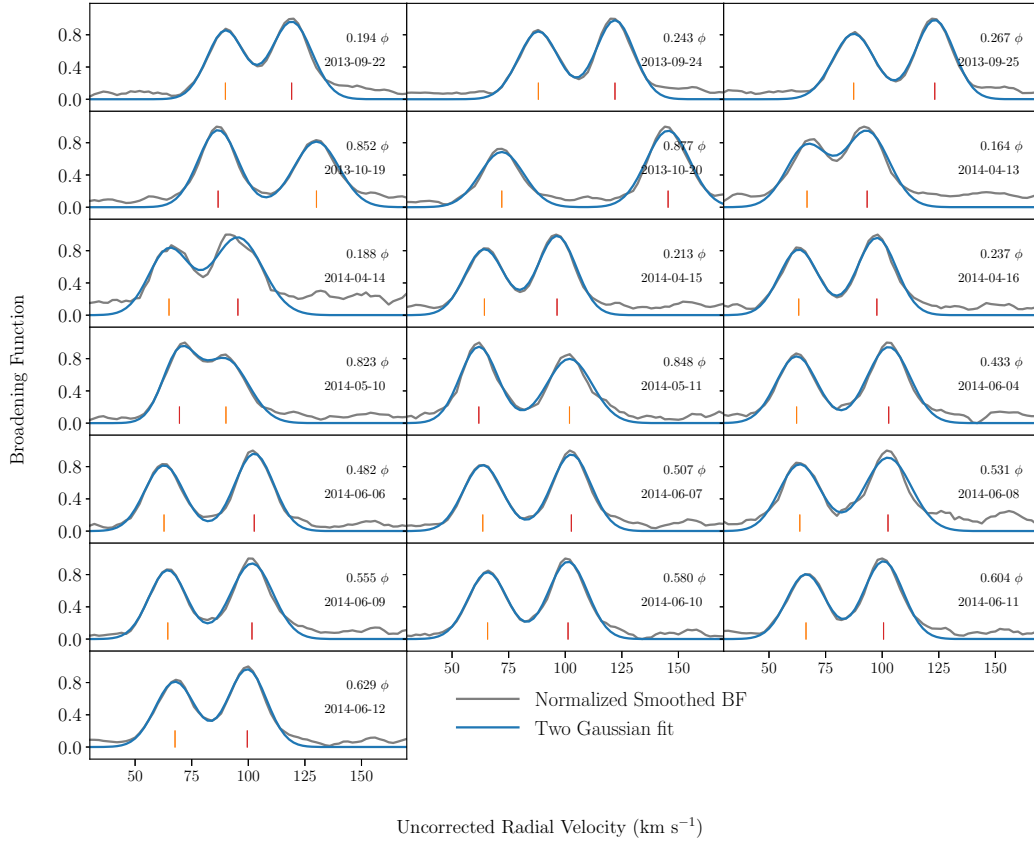


Figure 17. Same as Figure 16 but for KIC 6864859. In this case the primary (red) and secondary (orange) are less distinguishable due to the greater radius of the primary. Observations often were within a day of one another in their respective visit sets. Some visits were removed due to the presence of noise that could not be eliminated with our despiking method.

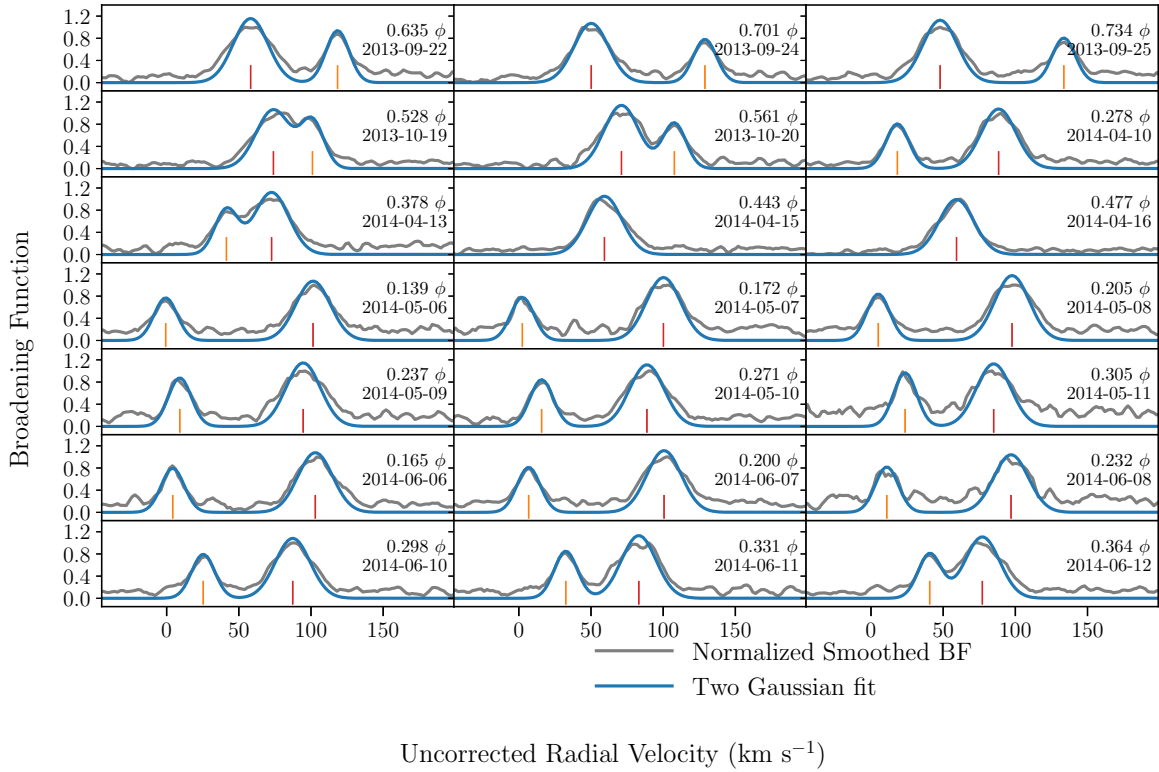


Figure 18. Same as Figure 16 but for KIC 6778289. In this case the primary (red) is slightly distinguishable from the secondary (orange), and the visit spectra were well separated over the course of the observations. Some visits were removed due to excess noise after having been ran through our despiking method.

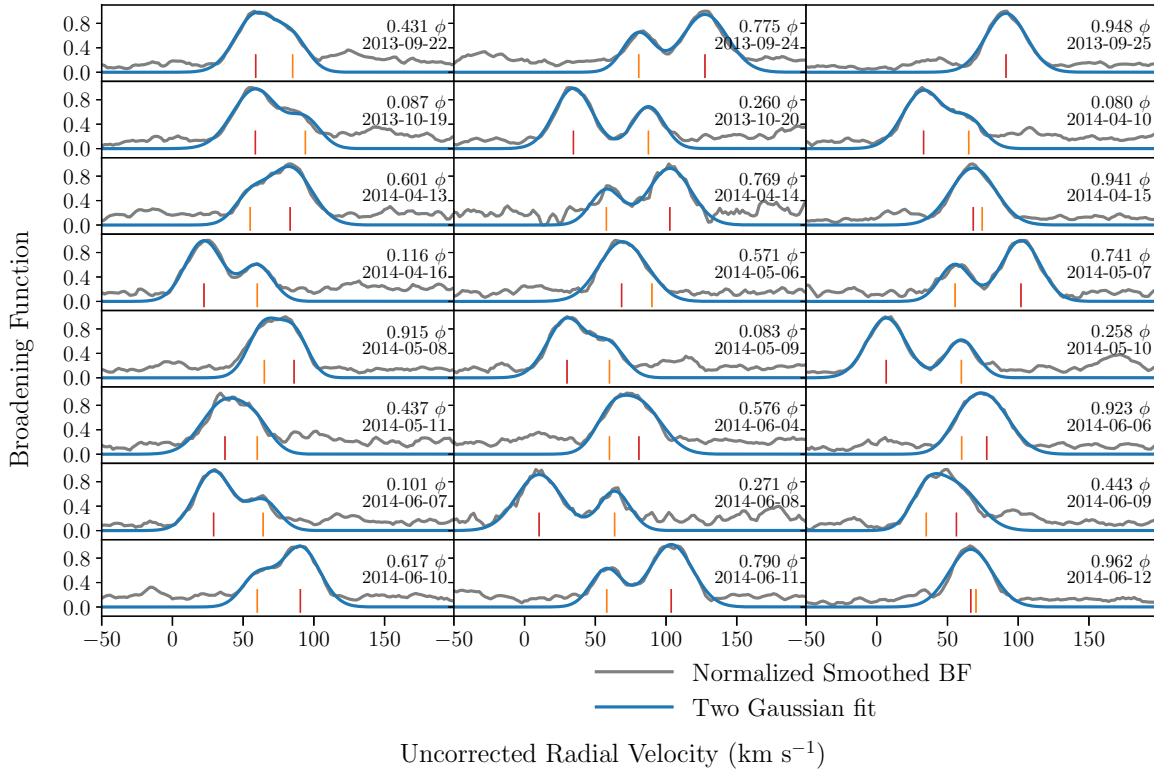


Figure 19. Same as Figure 16 but for KIC 6449358. In this case the primary (red) is easily distinguishable from the secondary (orange). This target had visits in which the primary and secondary were very close together but not directly on top of one another, in these occurrences error is more pronounced in the radial velocities extracted.

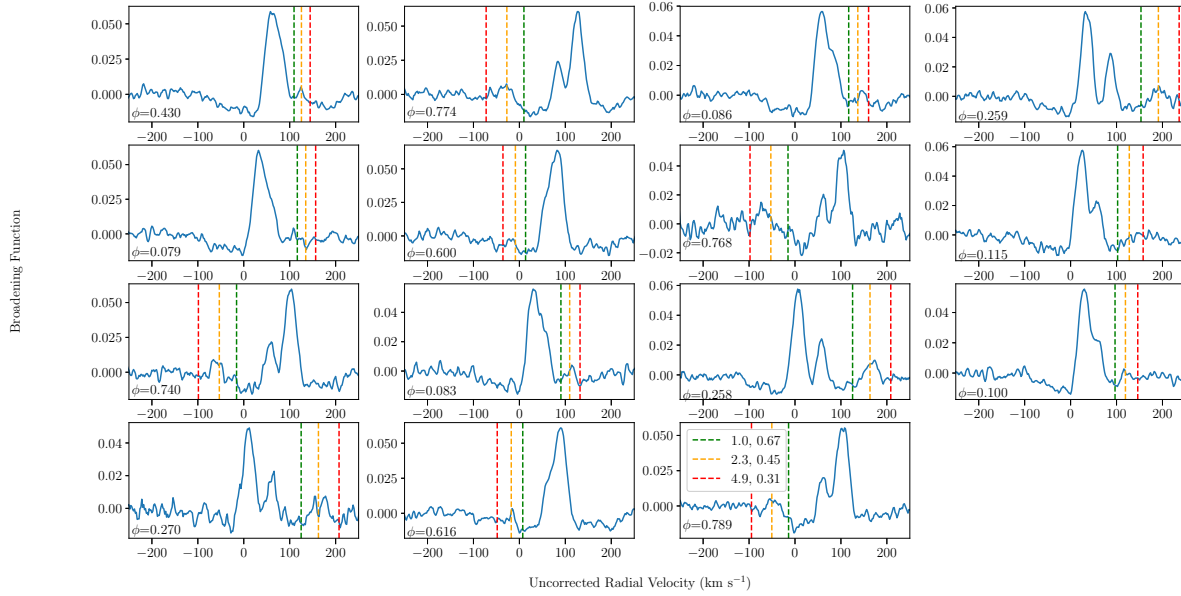


Figure 20. BF (blue solid line; zoomed out in each panel to $\pm 250 \text{ km s}^{-1}$) of KIC 6449358 overlotted with expected locations of the secondary component’s BF peak corresponding to various $M_1 + M_2, M_2/M_1$ combinations (green, orange, red dashed lines). In a few of the visits, tentative BF peaks coincide with the secondary’s expected locations for $M_1 + M_2 \sim 2.3, M_2/M_1 \sim 0.45$ (see, e.g., panels corresponding to phase=0.741, 0.083, 0.258, 0.259, 0.430). In general, however, additional BF “peaks” are lost in the noise of the spectra.

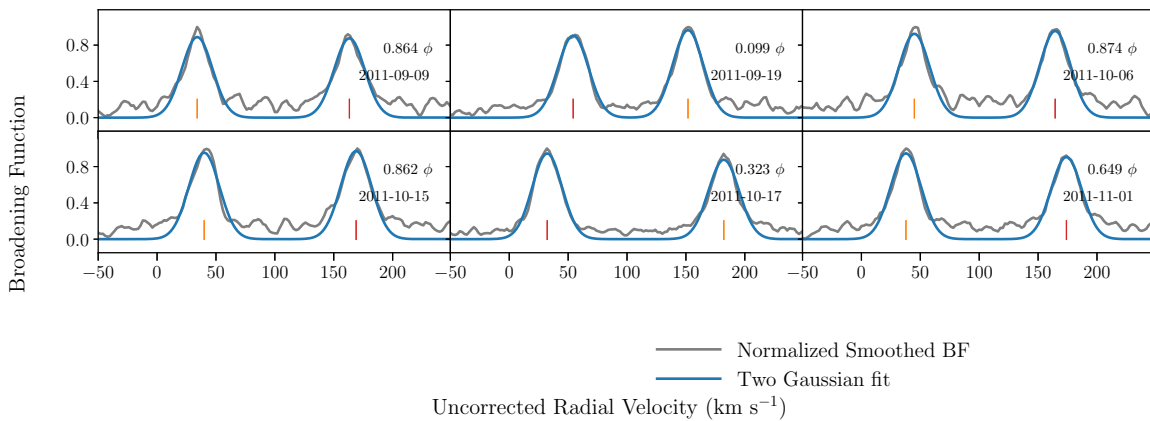


Figure 21. Same as Figure 16 but for KIC 4285087. In this case the primary (red) is easily distinguishable from the secondary (orange).

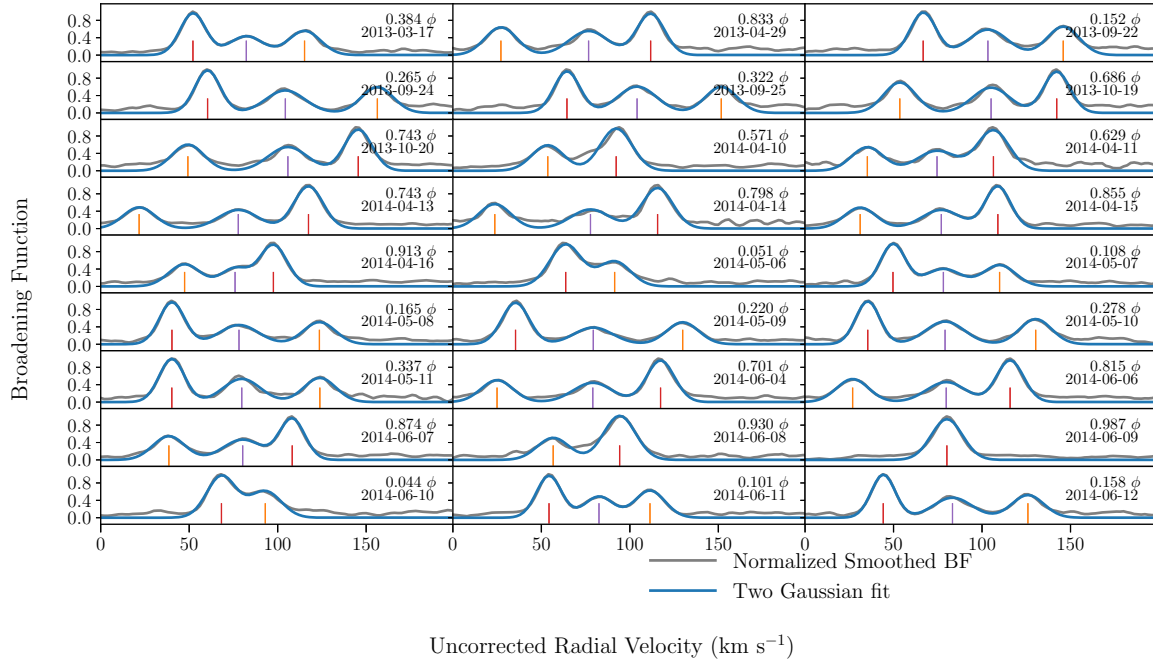


Figure 22. Same as Figure 16 but for KIC 6131659. In this case the primary (red) is very distinguishable from the secondary (orange). A tertiary (purple) member is visible but it does not show variance in its radial velocity component. In some panels the tertiary is not visible because it is very near to or within the primary or secondary peak.

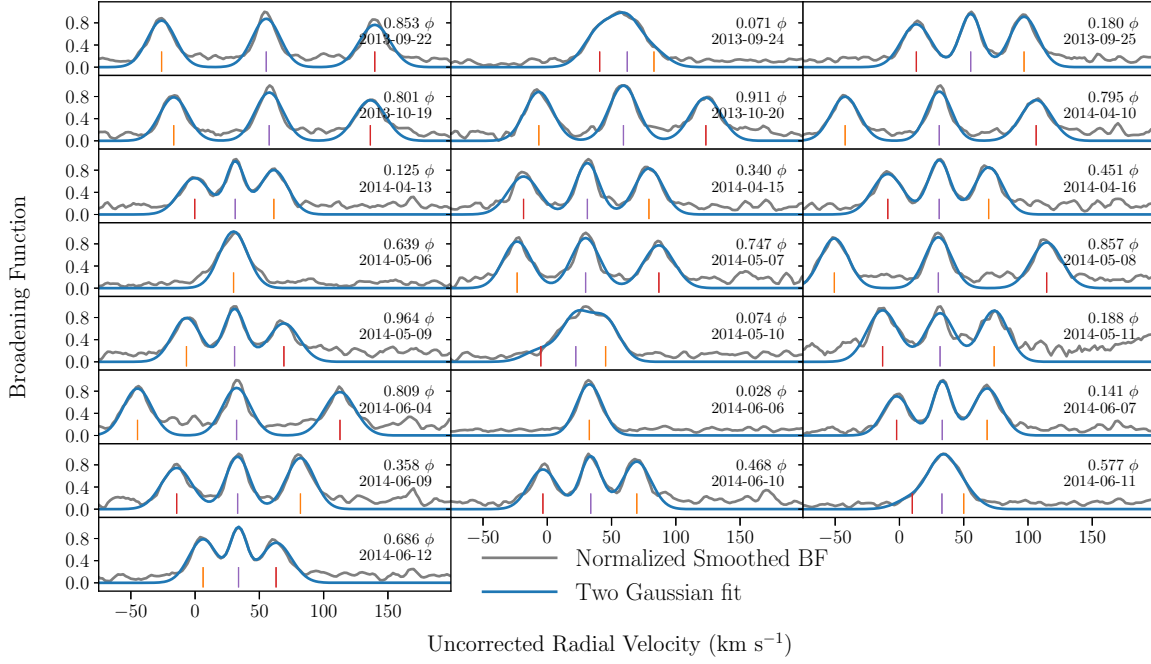


Figure 23. Same as Figure 16 but for KIC 6781535. In most panels, the primary (red) is very distinguishable from the secondary (orange). A tertiary member is present (purple) but is not RV variant.

Table 4. Measured radial velocities from APOGEE spectra

Time (BJD)	Orbital Phase	v_1 (km s ⁻¹)	v_2 (km s ⁻¹)
KIC 5285607			
2455813.69967	0.040	41.404 ± 0.101	86.618 ± 0.173
2455823.72647	0.611	118.406 ± 0.061	-3.961 ± 0.108
2455840.66112	0.954	88.218 ± 0.067	31.481 ± 0.109
2455849.57835	0.241	-24.927 ± 0.060	162.515 ± 0.105
2455851.64874	0.772	148.087 ± 0.060	...
2455866.56945	0.598	113.109 ± 0.063	2.025 ± 0.114
KIC 6864859			
2456557.73263	0.194	107.492 ± 0.058	...
2456559.72256	0.243	110.939 ± 0.079	78.670 ± 0.069
2456560.72029	0.267	112.129 ± 0.062	77.683 ± 0.056
2456584.63147	0.852	74.820 ± 0.060	117.933 ± 0.063
2456585.62998	0.877	57.225 ± 0.064	133.366 ± 0.052
2456760.90512	0.164	106.432 ± 0.072	80.051 ± 0.077
2456761.87222	0.188	108.904 ± 0.073	78.499 ± 0.079
2456762.86801	0.213	109.800 ± 0.057	77.234 ± 0.048
2456763.88053	0.237	111.281 ± 0.053	76.175 ± 0.054
2456787.80872	0.823	81.571 ± 0.078	104.978 ± 0.091
2456788.84246	0.848	76.011 ± 0.053	116.930 ± 0.062
2456812.75131	0.433	114.944 ± 0.053	73.779 ± 0.051
2456814.75480	0.482	114.257 ± 0.049	73.825 ± 0.050
2456815.78485	0.507	113.825 ± 0.053	73.899 ± 0.049
2456816.76560	0.531	113.034 ± 0.061	73.480 ± 0.061
2456817.76131	0.555	112.440 ± 0.056	74.591 ± 0.048
2456818.76390	0.580	111.523 ± 0.056	75.498 ± 0.054
2456819.76154	0.604	110.927 ± 0.058	75.851 ± 0.053
2456820.75533	0.629	109.049 ± 0.059	75.654 ± 0.066
KIC 6778289			
2456557.73261	0.635	47.229 ± 0.045	107.444 ± 0.045
2456559.72254	0.701	38.941 ± 0.049	117.686 ± 0.054
2456560.72027	0.734	36.535 ± 0.046	122.226 ± 0.053
2456584.63145	0.528	60.403 ± 0.059	87.443 ± 0.058
2456585.62996	0.561	57.486 ± 0.047	94.149 ± 0.053
2456757.89237	0.278	101.533 ± 0.048	31.407 ± 0.053
2456760.90514	0.378	85.993 ± 0.051	54.705 ± 0.056
2456762.86803	0.443	72.743 ± 0.049	...
2456763.88055	0.477	72.718 ± 0.052	...
2456783.83502	0.139	115.038 ± 0.049	12.937 ± 0.055
2456784.82136	0.172	113.771 ± 0.046	16.022 ± 0.055
2456785.82484	0.205	111.263 ± 0.044	18.581 ± 0.051
2456786.79785	0.237	108.112 ± 0.045	22.629 ± 0.048
2456787.80874	0.271	102.199 ± 0.047	29.240 ± 0.050
2456788.84248	0.305	98.364 ± 0.046	36.995 ± 0.044
2456814.75483	0.165	113.882 ± 0.048	15.109 ± 0.053
2456815.78487	0.200	111.327 ± 0.047	17.508 ± 0.052
2456816.76563	0.232	107.622 ± 0.050	21.517 ± 0.052
2456818.76392	0.298	97.639 ± 0.048	35.617 ± 0.053

Table 4 *continued*

Table 4 (continued)

Time (BJD)	Orbital Phase	v_1 (km s $^{-1}$)	v_2 (km s $^{-1}$)
2456819.76156	0.331	93.260 ± 0.046	42.669 ± 0.050
2456820.75535	0.364	87.120 ± 0.048	50.657 ± 0.054
KIC 6449358			
2456557.73275	0.431	47.972 ± 0.092	...
2456559.72268	0.775	116.332 ± 0.066	...
2456584.63158	0.087	44.828 ± 0.067	...
2456585.63008	0.260	20.640 ± 0.056	...
2456757.89224	0.080	46.407 ± 0.069	...
2456760.90501	0.601	96.766 ± 0.090	...
2456761.87212	0.769	116.275 ± 0.066	...
2456763.88043	0.116	36.021 ± 0.056	...
2456784.82126	0.741	115.987 ± 0.057	...
2456787.80865	0.258	20.638 ± 0.057	...
2456815.78483	0.101	40.477 ± 0.069	...
2456816.76558	0.271	21.538 ± 0.066	...
2456818.76389	0.617	101.418 ± 0.065	...
2456819.76152	0.790	114.484 ± 0.060	...
KIC 4285087			
2455813.69984	0.864	154.531 ± 0.062	25.294 ± 0.060
2455823.72663	0.099	43.398 ± 0.060	140.891 ± 0.056
2455840.66127	0.874	150.887 ± 0.057	31.327 ± 0.058
2455849.57849	0.862	154.496 ± 0.056	25.174 ± 0.057
2455851.64888	0.323	17.397 ± 0.057	167.332 ± 0.062
2455866.56955	0.649	158.478 ± 0.060	22.212 ± 0.057
KIC 6131659			
2456368.99876	0.384	62.544 ± 0.048	125.604 ± 0.091
2456411.91961	0.833	125.989 ± 0.045	41.382 ± 0.070
2456557.73279	0.152	55.739 ± 0.042	134.879 ± 0.069
2456559.72271	0.265	49.076 ± 0.041	145.012 ± 0.076
2456560.72045	0.322	52.988 ± 0.043	140.191 ± 0.075
2456584.63160	0.686	128.199 ± 0.045	39.531 ± 0.064
2456585.63010	0.743	131.456 ± 0.045	35.183 ± 0.075
2456757.89221	0.571	105.771 ± 0.047	67.116 ± 0.077
2456758.90157	0.629	120.004 ± 0.052	48.763 ± 0.084
2456760.90499	0.743	131.105 ± 0.044	35.406 ± 0.092
2456761.87209	0.798	129.464 ± 0.048	37.476 ± 0.080
2456762.86788	0.855	122.805 ± 0.042	45.003 ± 0.093
2456763.88040	0.913	111.491 ± 0.099	61.304 ± 0.105
2456783.83490	0.051	78.027 ± 0.051	105.677 ± 0.086
2456784.82125	0.108	63.945 ± 0.053	124.186 ± 0.111
2456785.82473	0.165	54.481 ± 0.042	137.809 ± 0.089
2456786.79774	0.220	49.620 ± 0.044	144.068 ± 0.089
2456787.80864	0.278	49.600 ± 0.040	144.493 ± 0.078
2456788.84238	0.337	54.269 ± 0.041	137.917 ± 0.082
2456812.75129	0.701	129.389 ± 0.044	36.993 ± 0.089
2456814.75479	0.815	127.626 ± 0.044	38.646 ± 0.085
2456815.78484	0.874	119.797 ± 0.047	50.101 ± 0.083
2456816.76560	0.930	105.694 ± 0.045	68.143 ± 0.089
2456817.76131	0.987	91.467 ± 0.048	...

Table 4 continued

Table 4 (*continued*)

Time (BJD)	Orbital Phase	v_1 (km s $^{-1}$)	v_2 (km s $^{-1}$)
2456818.76390	0.044	79.392 ± 0.046	...
2456819.76154	0.101	65.338 ± 0.047	122.387 ± 0.086
2456820.75533	0.158	55.054 ± 0.040	136.794 ± 0.088
KIC 6781535			
2456557.73097	0.853	128.940 ± 0.057	-37.069 ± 0.049
2456559.72097	0.071	29.463 ± 0.109	69.329 ± 0.204
2456560.71874	0.180	1.983 ± 0.057	85.464 ± 0.045
2456584.63091	0.801	122.687 ± 0.060	-30.426 ± 0.052
2456585.62946	0.911	109.784 ± 0.057	-20.436 ± 0.047
2456757.89316	0.795	119.307 ± 0.060	-29.253 ± 0.052
2456760.90580	0.125	12.366 ± 0.076	75.156 ± 0.060
2456762.86860	0.340	-4.835 ± 0.064	92.365 ± 0.049
2456763.88108	0.451	4.541 ± 0.060	82.610 ± 0.049
2456783.83465	0.639	...	43.811 ± 0.041
2456784.82095	0.747	100.401 ± 0.057	-9.574 ± 0.049
2456785.82438	0.857	128.143 ± 0.053	-37.060 ± 0.046
2456786.79735	0.964	82.332 ± 0.064	7.094 ± 0.053
2456787.80820	0.074	23.165 ± 0.158	62.731 ± 0.119
2456788.84189	0.188	1.170 ± 0.047	86.509 ± 0.045
2456812.74399	0.809	124.321 ± 0.056	-33.597 ± 0.049
2456814.75319	0.028	...	43.896 ± 0.046
2456815.78320	0.141	8.643 ± 0.068	79.192 ± 0.050
2456817.75959	0.358	-3.732 ± 0.059	92.410 ± 0.045
2456818.76215	0.468	7.142 ± 0.064	80.126 ± 0.049
2456819.75975	0.577	20.702 ± 0.354	57.626 ± 0.204
2456820.75351	0.686	73.353 ± 0.070	15.883 ± 0.061

REFERENCES

- Astropy Collaboration, Robitaille, T. P., Tollerud, E. J., et al. 2013, *A&A*, 558, A33
- Bailer-Jones, C. A. L., Rybizki, J., Fouesneau, M., Mantelet, G., & Andrae, R. 2018, *The Astronomical Journal*, 156, 58
- Bayless, A. J., & Orosz, J. A. 2006, *The Astrophysical Journal*, 651, 1155
- Borkovits, T., Hajdu, T., Sztakovics, J., et al. 2016, *MNRAS*, 455, 4136
- Borucki, W. J., Koch, D., Basri, G., et al. 2010, *Science*, 327, 977
- Bovy, J. 2016, *The Astrophysical Journal*, 817, 49
- Cohen, M., Wheaton, W. A., & Megeath, S. T. 2003, *AJ*, 126, 1090
- Conroy, K. E., Prša, A., Stassun, K. G., et al. 2014, *AJ*, 147, 45
- Czesla, S. 2018, ,
- Dotter, A., Chaboyer, B., Jevremović, D., et al. 2008, *The Astrophysical Journal Supplement Series*, 178, 89
- El-Badry, K., Rix, H.-W., Ting, Y.-S., et al. 2017, *MNRAS*, 473, 5043
- Fleming, S. W., Mahadevan, S., Deshpande, R., et al. 2015, *The Astronomical Journal*, 149, 143
- Foreman-Mackey, D., Hogg, D. W., Lang, D., & Goodman, J. 2013, *PASP*, 125, 306
- Foreman-Mackey, D., Hogg, D. W., Lang, D., & Goodman, J. 2013, *PASP*, 125, 306
- Gaulme, P., McKeever, J., Jackiewicz, J., et al. 2016, *The Astrophysical Journal*, 832, 121
- Ginsburg, A. 2017, ,
- Hunter, J. D. 2007, *Computing In Science & Engineering*, 9, 90
- Husser, T.-O., von Berg, S. W., Dreizler, S., et al. 2013, *Astronomy & Astrophysics*, 553, A6
- Jones, E., Oliphant, T., Peterson, P., et al. 2001, *SciPy: Open source scientific tools for Python*, ,
- Kipping, D. M. 2010, *Monthly Notices of the Royal Astronomical Society*, 408, 1758
- Kipping, D. M. 2013, *Astronomy and Astrophysics*, 154, 216

- Kirk, B., Conroy, K., Prsa, A., et al. 2016, *The Astronomical Journal*, 151, 68
- Kozai, Y. 1962, *The Astronomical Journal*, 67, 591
- Lehmann, H., Zechmeister, M., Dreizler, S., Schuh, S., & Kanzler, R. 2012, *Astronomy and Astrophysics*, 541, A105
- Lu, W., Rucinski, S. M., & OgŁoza, W. 2001, *The Astronomical Journal*, 122, 402
- Majewski, S. R., Schiavon, R. P., Frinchaboy, P. M., et al. 2015, [arXiv.org](https://arxiv.org/abs/1509.05420v1), 1509.05420v1
- Mandel, K., & Agol, E. 2002, *The Astrophysical Journal*, 580, L171
- Matson, R. A., Gies, D. R., Guo, Z., & Williams, S. J. 2017, *The Astronomical Journal*, 154, 216
- McKinney, W. 2010, in *Proceedings of the 9th Python in Science Conference*, ed. S. van der Walt & J. Millman, 51 – 56
- Morton, T. D., Bryson, S. T., Coughlin, J. L., et al. 2016, *The Astrophysical Journal*, 822, 86
- Newville, M., Stensitzki, T., Allen, D. B., et al. 2016, *Astrophysics Source Code Library*, ascl:1606.014
- Nidever, D. L., Holtzman, J. A., Prieto, C. A., et al. 2015, *The Astronomical Journal*, 150, 173
- Pérez, A. E. G., Prieto, C. A., Holtzman, J. A., et al. 2016, *The Astronomical Journal*, 151, 144
- Pinsonneault, M. H., Elsworth, Y., Epstein, C., et al. 2014, *The Astrophysical Journal Supplement Series*, 215, 19
- Pinsonneault, M. H., Elsworth, Y. P., Tayar, J., et al. 2018, *ArXiv e-prints*, [arXiv:1804.09983](https://arxiv.org/abs/1804.09983)
- Price-Whelan, A., Mechev, A., & jumeroag. 2018, [adrn/makecite: v0.1, , , doi:10.5281/zenodo.1343295](https://doi.org/10.5281/zenodo.1343295)
- Price-Whelan, A. M., Sipócz, B. M., Günther, H. M., et al. 2018, *AJ*, 156, 123
- Rappaport, S., Deck, K., Levine, A., et al. 2013, *ApJ*, 768, 33
- Rawls, M. L., Gaulme, P., McKeever, J., et al. 2016, *The Astrophysical Journal*, 818, 108
- Rucinski, S. M. 1992, *The Astronomical Journal*, 104, 1968
- . 1999, *International Astronomical Union Colloquium*, 170, 82
- . 2002, *The Astronomical Journal*, 124, 1746
- . 2004, *Symposium - International Astronomical Union*, 215, 17
- Skrutskie, M. F., Cutri, R. M., Stiening, R., et al. 2006, *AJ*, 131, 1163
- Stassun, K. G., Collins, K. A., & Gaudi, B. S. 2017, *AJ*, 153, 136
- Stassun, K. G., Mathieu, R. D., & Valenti, J. A. 2007, *The Astrophysical Journal*, 664, 1154
- Stassun, K. G., & Torres, G. 2018, *ApJ*, 862, 61
- Thompson, S. E., Everett, M., Mullally, F., et al. 2012, *ApJ*, 753, 86
- Tokovinin, A., Thomas, S., Sterzik, M., & Udry, S. 2006, *Astronomy and Astrophysics*, 450, 681
- Tokovinin, A. A. 1997, *Astronomy Letters*, 23, 727
- Torres, G., Andersen, J., & Giménez, A. 2010, *A&A Rv*, 18, 67
- Torres, G., Curtis, J. L., Vanderburg, A., Kraus, A. L., & Rizzuto, A. 2018, [arXiv.org](https://arxiv.org/abs/1808.07482), [arXiv:1808.07482](https://arxiv.org/abs/1808.07482)
- Van Der Walt, S., Colbert, S. C., & Varoquaux, G. 2011, *ArXiv e-prints*, [arXiv:1102.1523](https://arxiv.org/abs/1102.1523)
- Windemuth, D., Agol, E., Ali, A., & Kiefer, F. 2018, *MNRAS*